

AD-A253 413



WL-TR-92-3018

STIC  
ELECTE  
JUL 16 1992  
C D



**High-Speed Viscous Flows Past Blunt Bodies and Compression Corners with  
Flux-Split Methods**

Datta Gaitonde  
Universal Energy Systems  
4401 Dayton-Xenia Road  
Dayton, OH 45432-1894

March 1992

Final Report for Period October 1990 - November 1991

Approved for public release; distribution is unlimited.

92-18813



FLIGHT DYNAMICS DIRECTORATE  
WRIGHT LABORATORY  
AIR FORCE SYSTEMS COMMAND  
WRIGHT-PATTERSON AIR FORCE BASE, OHIO 45433-6553

92 7 15 009

## NOTICE

When Government drawings, specifications, or other data are used for any purpose other than in connection with a definitely Government-related procurement, the United States Government incurs no responsibility or any obligation whatsoever. The fact that the government may have formulated or in any way supplied the said drawings, specifications, or other data, is not to be regarded by implication, or otherwise in any manner construed, as licensing the holder, or any other person or corporation; or as conveying any rights or permission to manufacture, use, or sell any patented invention that may in any way be related thereto.

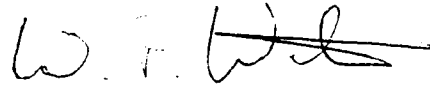
This report is releasable to the National Technical Information Service (NTIS). At NTIS, it will be available to the general public, including foreign nations.

This technical report has been reviewed and is approved for publication.



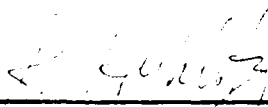
---

DATTA GAITONDE  
Visiting Scientist



---

W.P. WEBSTER  
Actg. Technical Manager  
Computational Aerodynamics



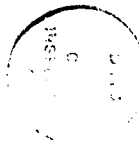
---

Col. R. HERKLOTZ  
Chief  
Aeromechanics Division

If your address has changed, if you wish to be removed from our mailing list, or if the addressee is no longer employed by your organization please notify WL/FIMM WPAFB, OH 45433-6553 to help us maintain a current mailing list.

Copies of this report should not be returned unless return is required by security considerations, contractual obligations, or notice on a specific document.

REPORT DOCUMENTATION PAGE			Form Approved OMB No. 0704-0188	
Public reporting burden for this collection of information is estimated to average 1 hour per response, including the time for reviewing instructions, searching existing data sources, gathering and maintaining the data needed, and completing and reviewing the collection of information. Send comments regarding this burden estimate or any other aspect of this collection of information, including suggestions for reducing this burden, to Washington Headquarters Services, Directorate for Information Operations and Reports, 1215 Jefferson Davis Highway, Suite 1204, Arlington, VA 22202-4302, and to the Office of Management and Budget, Paperwork Reduction Project (0704-0188), Washington, DC 20503.				
1. AGENCY USE ONLY (Leave blank)	2. REPORT DATE March 1992	3. REPORT TYPE AND DATES COVERED Final, Oct. 90-Nov. 91		
4. TITLE AND SUBTITLE High-Speed Viscous Flows Past Blunt Bodies and Compression Corners with Flux-Split Methods		5. FUNDING NUMBERS F33615-88-C-2908 PE-61102F PR-2307 TA-N6 WU-11		
6. AUTHOR(S) Datta Gaitonde				
7. PERFORMING ORGANIZATION NAME(S) AND ADDRESS(ES) Universal Energy Systems 4401 Dayton-Xenia Rd Dayton, OH 45432-1894		8. PERFORMING ORGANIZATION REPORT NUMBER		
9. SPONSORING/MONITORING AGENCY NAME(S) AND ADDRESS(ES) Joseph Shang (513-255-6156) Flight Dynamics Directorate (WL/FIMM) Wright Laboratory Wright-Patterson AFB, OH 45433-6553		10. SPONSORING/MONITORING AGENCY REPORT NUMBER  WL-TR-92-3018		
11. SUPPLEMENTARY NOTES				
12a. DISTRIBUTION/AVAILABILITY STATEMENT Approved for Public Release; Distribution is Unlimited.		12b. DISTRIBUTION CODE		
13. ABSTRACT (Maximum 200 words) This effort investigates the accuracy of some flux-split algorithms in high-speed viscous flows. Three methods are examined: 1) MacCormack and Candler's (MC) scheme, 2) the van Leer (vL) scheme and 3) the method of Roe. The problems studied include the blunt body flow at Mach 16 and the flow past a 24° compression corner at Mach 14. Higher order accuracy is obtained with the MUSCL approach. Viscous terms are centered in the full Navier-Stokes cell-centered implicit finite volume simulation. The results indicate a relative similarity of predicted surface pressure with all methods on both flows. However, considerable disparity exists in heat transfer prediction especially on the coarser meshes with van Leer's splitting exhibiting the most overprediction. Generally however, this disparity diminishes as the grid is refined. The occurrence of anomalous carbuncle solutions with Roe's scheme may be suppressed with appropriate increase in entropy cutoff with no significant penalty in accuracy. For the ramp flow, the MC method predicts the size of the separated flow region most accurately, though some overprediction of heat transfer is observed. Roe's algorithm, and on the finer grids, van Leer's method also exhibit comparable results.				
14. SUBJECT TERMS Flux-Split; Viscous; High-Speed; Blunt Body; Corner			15. NUMBER OF PAGES 60	
			16. PRICE CODE	
17. SECURITY CLASSIFICATION OF REPORT Unclassified	18. SECURITY CLASSIFICATION OF THIS PAGE Unclassified	19. SECURITY CLASSIFICATION OF ABSTRACT Unclassified	20. LIMITATION OF ABSTRACT UL	



Accession for	
NTIS (GAI)	<input checked="" type="checkbox"/>
DTIC TAB	<input type="checkbox"/>
Unannounced	<input type="checkbox"/>
Justification	
By	
Distribution/	
Availability Codes	
Dist	Avail and/or Special
A-1	

## Contents

List of Figures . . . . .	iv
List of Tables . . . . .	v
Acknowledgements . . . . .	vi
1 Introduction . . . . .	1
2 Theoretical Model . . . . .	7
2.1 MacCormack and Candler Flux-Vector Split Algorithm . . . . .	9
2.2 van Leer's Flux-Vector Split Algorithm . . . . .	12
2.3 Roe's Flux-Difference Split Algorithm . . . . .	13
3 Boundary Conditions and Numerical Details . . . . .	15
4 Blunt Body Flow . . . . .	17
4.1 Flow Parameters and Grid Details . . . . .	17
4.2 Results . . . . .	18
5 Corner Flow . . . . .	35
5.1 Flow Parameters and Grid Details . . . . .	35
5.2 Results . . . . .	35
6 Conclusions . . . . .	45
7 References . . . . .	46
Nomenclature . . . . .	51

## List of Figures

1	Schematic of corner flow . . . . .	5
2	Grids employed . . . . .	6
3	Surface pressure in Mach 16 flow past a blunt body with the MC scheme . . . . .	19
4	Heat transfer in Mach 16 flow past a blunt body with the MC scheme . . . . .	21
5	Mach number along stagnation streamline for Mach 16 flow past a blunt body with the MC scheme . . . . .	22
6	Contours for blunt body flow with the MC scheme . . . . .	23
7	Surface pressure in Mach 16 flow past a blunt body with the van Leer scheme . . . . .	25
8	Heat transfer in Mach 16 flow past a blunt body with the van Leer scheme . . . . .	26
9	Mach number along stagnation streamline for Mach 16 flow past a blunt body with the van Leer scheme . . . . .	27
10	Contours for blunt body flow with the van Leer scheme . . . . .	28
11	Effect of extrapolation of different variables on surface quantities with the van Leer scheme . . . . .	29
12	Surface pressure in Mach 16 flow past a blunt body with the Roe scheme . . . . .	30
13	Heat transfer in Mach 16 flow past a blunt body with the Roe scheme . . . . .	32
14	Mach number along stagnation streamline for Mach 16 flow past a blunt body with the Roe scheme . . . . .	33
15	Contours for blunt body flow with the Roe scheme . . . . .	34
16	Comparison of pressure coefficient for compression corner flow . . . . .	38
17	Comparison of heat transfer coefficient for compression corner flow . . . . .	39
18	Comparison of skin friction coefficient for compression corner flow . . . . .	41
19	Mach contours for compression corner flow on Grid 4 . . . . .	42

## List of Tables

4.1	Blunt body grid details . . . . .	18
5.1	Corner grid details . . . . .	36
5.2	Separation region details for corner flow . . . . .	44

## **Acknowledgements**

Computations were performed on computers at WPAFB and the NAS program. The support and assistance of the staff at both locations are gratefully acknowledged.

## 1. Introduction

Several algorithms have been described in the literature for the numerical representation of the inviscid flux in the Navier-Stokes equations. The more recent of these schemes have their underlying basis in either mathematical (for example TVD schemes [1]) or physical (for example flux-splitting [2, 3]) analyses. All of these modern methods employ upwinding in one form or another to obtain algorithms possessing better dissipation characteristics, higher stability bounds and increased numerical efficiency [4, 5]. This inherently dissipative nature of upwind schemes is beneficial at or near shock waves where the inviscid fluxes dictate finite jumps in flow variables. However, typical *viscous* supersonic flows about bodies display steep gradients not only in shock regions but also in the boundary layers. The dissipative characteristics of upwind schemes in these latter regions is a drawback since the numerical dissipation may be comparable to or overwhelm the viscous terms. This can often have detrimental consequences on the prediction of heat transfer rates [6].

Following the approach of several authors [7, 8] upwind schemes may be classified according to the Riemann solver used to evaluate the fluxes at the cell faces and the mechanism through which higher order spatial accuracy is obtained — non-MUSCL or MUSCL. Some examples of schemes obtaining higher order accuracy with non-MUSCL approaches are the “Symmetric” TVD scheme of Yee [9, 10] and the “Upwind” TVD scheme of Harten and Yee [10, 11] where the quotes indicate the fact these words do not retain the traditional centered or upwind meanings because of the presence of flux functions and slope limiters.

The focus of the present research is on schemes that obtain higher order accuracy through the MUSCL approach of van Leer [12]. Specifically, we study the performance of the flux vector split methods of MacCormack and Candler [6] (to be abbreviated henceforth as the **MC** method) and van Leer [3] (abbreviated **vL**) and the flux difference split method of Roe [13]. The distinction between flux-*vector* and flux-*difference* splitting may be based upon the model used to derive the basic interaction between neighboring cells. When the interaction between neighboring cells is modeled with finite-amplitude waves (the Riemann approach), the scheme is called flux-difference



splitting; when accomplished through the mixing of pseudo-particles (the Boltzmann approach) the method is called flux-vector splitting [3].

The original Steger-Warming flux-vector split method [2] (often called the beam scheme) exploits the homogeneity of the inviscid flux vector to split the flux into positive and negative components depending upon the sign of the local eigenvalues. Since the mass flux for this scheme is not continuous where the eigenvalues change sign, “glitches” are often observed at sonic and stagnation points. This method was proven to be excessively dissipative in the boundary layers by MacCormack and Candler [6] who suggest relatively simple changes (outlined later) to eliminate numerical diffusion: these modifications give rise to the MC method. Reported applications of the original Steger-Warming algorithm include inviscid flows past airfoils [2] and cylinders [14]. The MC scheme has previously been applied for flat plate boundary layer flows, flows past compression ramps, blunt body flows [6], viscous real gas flows past sphere-cones [15], Type *III*<sup>+</sup> and Type *IV* viscous shock-shock interactions [16].

Unlike Steger Warming splitting, van Leer’s formula exhibits flux continuity across eigenvalue sign changes. Some improvement is obtained in shock capture capability over the Steger Warming method [17]. Applications with van Leer’s scheme include inviscid subsonic and transonic flows over airfoils [18], viscous shock-induced separated flows [19], flows over delta wings [20] and recently a Type *III*<sup>+</sup> interaction at Mach 8 [21] with and without a turbulence model. A comparison of the van Leer and the original Steger-Warming scheme for some Euler flows may be found in Anderson *et al.* [17].

Roe’s flux-difference split method [13] is based upon accurate prediction of wave interactions between interfaces through an approximate (linearized) equation. This approach has been demonstrated to reduce the numerical dissipation [22] and has subsequently been extended to reduce grid-dependence [23] common to methods based on 1-D analysis. One drawback of this algorithm is the possible violation of the entropy condition, necessitating the employment of appropriate entropy correction factors. One approach is described in considerable detail in Chapter 2. Roe’s flux difference split method has been applied in recent years for viscous and inviscid conical flow [13], nozzle flow and shock reflection [24].

The popularity of the above three flux split methods in the computation of high speed flows is likely to increase especially with their extensions to include high temperature effects by Liu and Vinokur [25], Grossman and Cinnella [26, 27] and Shuen *et al.* [28]. A comparison of the relative merits of each of these schemes has been performed either on inviscid flows [17, 8] or on simple viscous flows [22, 29]. The former type of comparison focuses exclusively upon shock capture capability while the latter is restricted to relatively simple flows (e.g., flat plate boundary layers). An overall assessment of these methods based upon the studies available in the literature is further complicated by the ambiguity in specific implementation.

We perform a detailed analysis, with grid resolution study, of the prediction capabilities of these three algorithms on two classic 2-D viscous laminar problems with specific emphasis in the prediction of heat transfer rates. The implementation of each algorithm is determined for our purposes to be the one most commonly utilized as observed in the literature. The choice of problems and flow parameters is dictated by the need to simulate features generic to a wide range of complex flows for which reliable experimental data in the form of surface pressure and heat transfer are available.

- Mach 16 Blunt body flow: This is a classic problem typified by a simple geometry and flow features and the availability of a relatively accurate theoretical value of stagnation heat transfer [30]. Despite the relative simplicity of the flowfield, several algorithms have displayed difficulties in heat transfer prediction. These difficulties generally manifest themselves as the so-called “carbuncle” or “bulge” phenomenon [31, 32, 33] and may be the result of the singularity of the eigenvalues across the entire length of the line of symmetry.
- Mach 14 flow past a compression ramp: This type of flow exists generically in several practical applications (e.g., inlets) and is typical of shock-wave boundary layer interactions (Fig. 1). The parameters chosen duplicate one of the experiments of Holden and Moselle [34] corresponding to a  $24^\circ$  ramp at Mach 14.1. The resultant flowfield is known to exhibit a large region of recirculation [35]. Although some evidence exists to suggest that 3-D effects may be important [36], no effort is made to resolve this issue in the present work.

In each instance, a sequence of grids is employed to obtain grid resolution studies. The finest grids utilized are presented in Fig. 2. Further quantitative details are presented and discussed with the results.

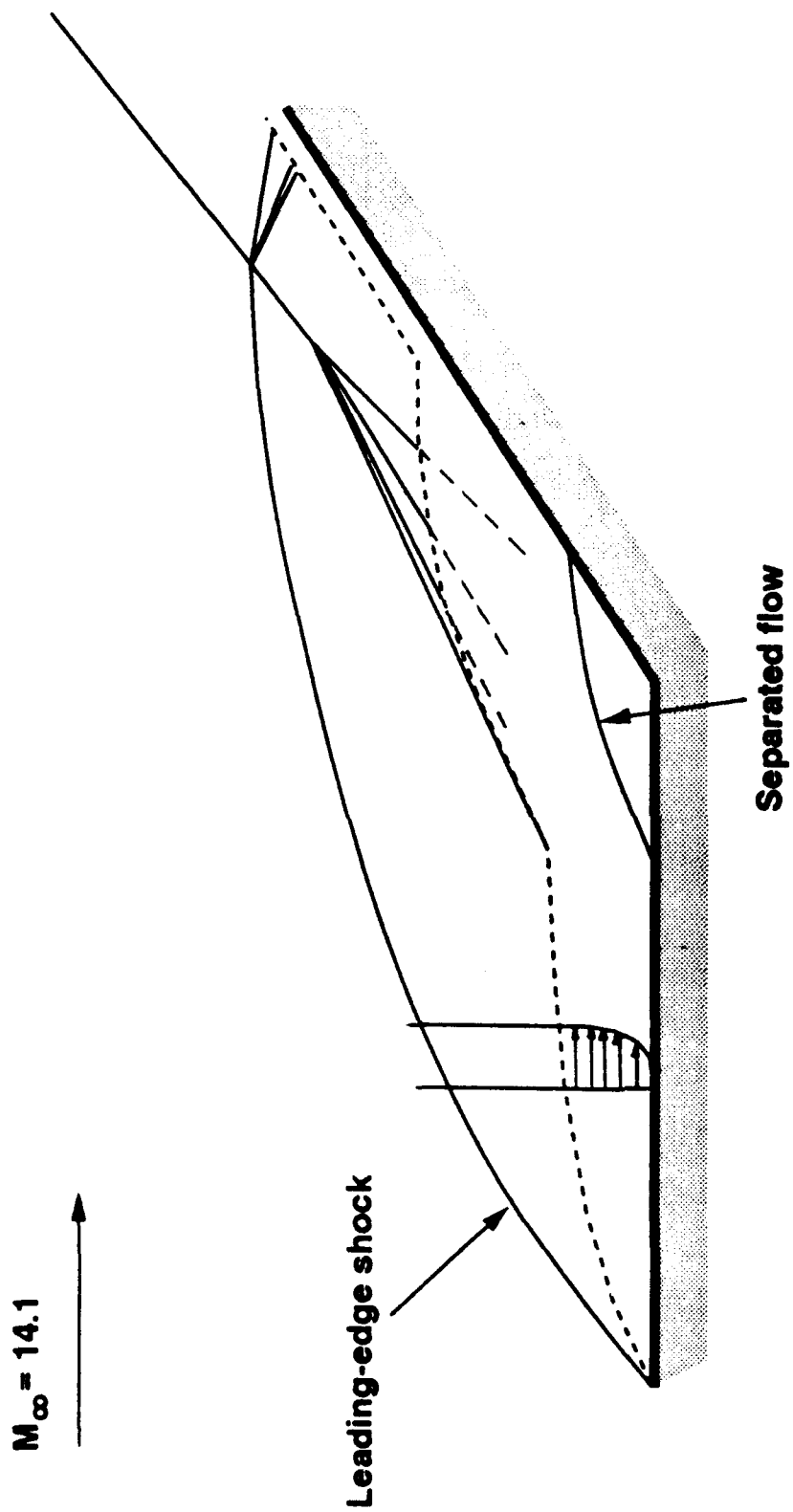
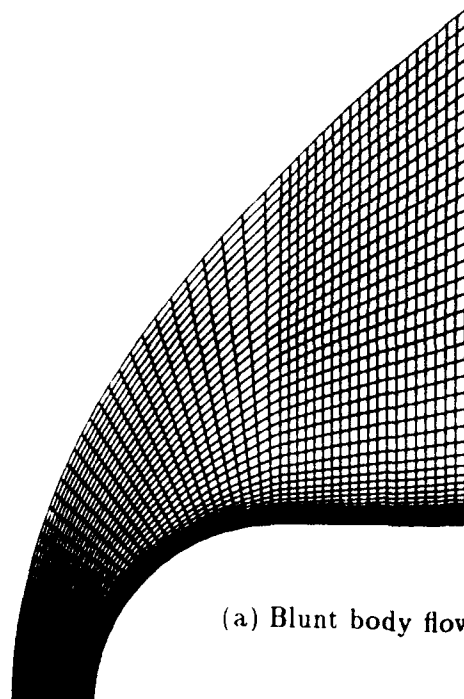
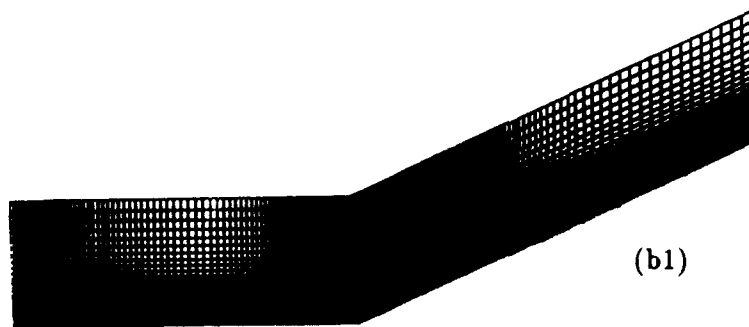


Figure 1: Schematic of corner flow



(a) Blunt body flow



(b1)



(b2)

(b) Corner flow

Figure 2: Grids employed

## 2. Theoretical Model

The 2-D Navier Stokes equations in strong conservation form are solved in the transformed  $(\xi, \eta)$  coordinates:

$$\frac{\partial \hat{U}}{\partial t} + \frac{\partial \hat{F}}{\partial \xi} + \frac{\partial \hat{G}}{\partial \eta} = 0 \quad (2.1)$$

where  $\hat{U}$  is the solution vector of conserved variables ( $\{\rho, \rho u, \rho v, \rho e\}/J$ ) with  $\rho$  denoting density,  $u$  and  $v$  the Cartesian components of velocity,  $e$  the total energy per unit mass ( $= e_i + 0.5(u^2 + v^2)$ ) and  $e_i$  the internal energy per unit mass ( $= C_v T$ ) where  $C_v$  is the specific heat at constant volume and  $T$  is the static temperature. The flux vectors,  $\hat{F}$  and  $\hat{G}$ , include the full viscous and inviscid terms,  $\xi(x, y)$  and  $\eta(x, y)$  are the transformed variables. For the configurations under consideration, the  $\xi$  coordinate lines are in the generally circumferential or streamwise direction while the  $\eta$  lines are radial or body-normal. The density, static pressure  $p$  and temperature are related through the equation of state  $p = \rho R T$  where  $R$  is the gas constant. The molecular viscosity  $\mu$  is approximated by Sutherland's law and the molecular Prandtl number  $Pr$  is assumed to be 0.73 (air).

Equation 2.1 may be interpreted as describing the balance of mass, momentum and energy over an arbitrary control volume [18]. Numerical time integration is achieved with a residual driven line Gauss-Seidel relaxation scheme as described in the works of MacCormack [37] and Candler [38]. With first-order backward Euler time discretization and linearization of the fluxes in time, the discretized equation may be written in the form:

$$\{NUMERICS\} \delta \bar{U} = PHYSICS \quad (2.2)$$

where *PHYSICS* represents the residual and *NUMERICS* contains the driving terms and  $\delta \bar{U}$  represents the change in the solution vector at each time step. The full Navier-Stokes equations are utilized in computing the residual with the appropriate upwind model for the inviscid terms and centered evaluation of the viscous terms. One advantage of the above methodology is that approximations may be utilized in the *NUMERICS* portion of the code without affecting the accuracy of the converged result. In fact, Liou and van Leer [24] point out that even if the *PHYSICS*

term is evaluated with other methods (such as van Leer's splitting or Roe's upwinding), the use of Steger Warming splitting in evaluating the *NUMERICS* portion leads to robust codes for the Newton linearization procedure. The implicit operator in this research therefore utilizes the Steger Warming Jacobians to obtain strong diagonal dominance. Further, for simplicity the viscous Jacobians in the driving *NUMERICS* portion are computed with the thin layer approximation.

When solved with the Gauss-Seidel line relaxation procedure, Eqn. 2.2 represents a block tridiagonal system. For transonic and supersonic flows, line relaxation methods are superior to approximate factorization methods in convergence rate which amply compensates for the larger computation required per iteration [39]. The line Gauss-Seidel algorithm is also unconditionally stable in the linear analysis and is known to be relatively insensitive to the choice of time increment per iteration.

For most computations, the automatic CFL number adjustment algorithm of MacCormack [40] is utilized. In this, the allowable time step is automatically permitted to double every  $n_{it}$  iterations from an initial value (typically small  $\sim 0.01$ ). After the explicit part of each iteration (the first stage if a two-stage method is used), the changes in the solution are adjusted so that the maximum relative change in density at any point due to the present iteration is always less than a fixed value ( $\delta\rho_{max}$  say) and the maximum relative *decrease* in temperature is also less than another fixed value ( $\delta T_{min}$  say). This adjustment involves the division of the residual at each point by a fixed number determined such that the above conditions are satisfied. In effect, this cuts the explicit allowable timestep by cutting the CFL. Although MacCormack obtained arbitrary increases in the CFL number, for some of the current computations, the residuals as well as CFL numbers asymptote to limit cycles. In such instances, the maximum CFL is restricted to such a value that the CFL number remains stable and the solution residual converges. This typically eliminates the high frequency oscillations in the residual cycles. Also, although MacCormack used maximum allowable relative change values ( $|\delta\rho/\rho|_{max}$  or  $-\delta T/T|_{max}$ ) of 0.5, in the present instance, especially for finer grids, values of 0.01 to 0.05 were used.

A brief description of each algorithm is presented with reference to the flux evaluation ( $\hat{G}$ ) at a  $j + \frac{1}{2}$  surface in the present cell centered finite volume formulation. Denoting the derivatives

of the transformed coordinates with respect to the physical coordinates as  $\xi_x, \xi_y$  etc., the flux at this surface in generalized coordinates is:

$$\hat{G} = J^{-1} (\eta_x \bar{F} + \eta_y \bar{G}) \quad (2.3)$$

where  $J$  is the Jacobian,  $\bar{F}$  and  $\bar{G}$  are the fluxes expressed in Cartesian coordinates and include viscous and inviscid components:

$$\bar{F} = F + F_v \quad \text{and} \quad \bar{G} = G + G_v \quad (2.4)$$

with  $F$  and  $G$  representing Cartesian inviscid fluxes and  $F_v$  and  $G_v$  the viscous fluxes respectively. The viscous fluxes are evaluated in a centered fashion and will not be discussed extensively. The vectors  $\text{grad}(\xi)/J$  and  $\text{grad}(\eta)/J$  represent the directed areas of cell interfaces in the  $\xi, \eta$  and  $\zeta$  directions and  $J$  is the inverse cell volume. Since the extension to general coordinates is straightforward as described by Anderson *et al.* [17], the following discussion focuses only on the inviscid Cartesian flux vector  $G$ .

At each interface, the state of the flow is described by two vectors of conserved variables,  $U^L$  and  $U^R$  on either side of the interface. These vectors are obtained from the known values at the cell centers with the MUSCL approach in conjunction with a limiter as described below.

## 2.1 MacCormack and Candler Flux-Vector Split Algorithm

In flux vector splitting, the inviscid flux is split into positive and negative components for appropriate upwind differencing:

$$G_{j+\frac{1}{2}} = G^+(U_{j+\frac{1}{2}}^L) + G^-(U_{j+\frac{1}{2}}^R) \quad (2.5)$$

We describe first the original Steger Warming method and then the MacCormack and Candler scheme. In the Steger Warming approach [2] (abbreviated OSW), since the inviscid fluxes are first order homogeneous and hyperbolic, the flux Jacobian  $B$  ( $B = \partial G / \partial U$ ,  $G = BU$ ) may be written as:

$$B = Q^{-1} \Lambda Q = Q^{-1} (\Lambda^+ + \Lambda^-) Q = B^+ + B^- \quad (2.6)$$



where  $\Lambda$  is a diagonal matrix consisting of the eigenvalues of  $B$  ( $\Lambda = \text{diag}\{v, v+c, v-c\}$ ) and  $\Lambda^+$  and  $\Lambda^-$  denote the splitting of the eigenvalues into positive and negative components. For convenience, the matrix  $Q$  may be written as [38]:

$$Q = CS \quad (2.7)$$

where  $S = \frac{\partial V}{\partial U}$ ,  $V$  is the vector of nonconserved variables  $\{\rho, u, v, p\}$  and  $C$  diagonalizes the flux vector  $G$  written in terms of  $V$ . At a face  $j + 1/2$  therefore, the inviscid original Steger Warming flux ( $G_{OSW}$ ) may be written as:

$$G_{OSW, j+\frac{1}{2}} = B_j^+ U^L + B_{j+1}^- U^R \quad (2.8)$$

For second order accuracy, the vectors of conserved variables,  $U^L$  and  $U^R$ , are obtained at the cell interfaces by extrapolation to the cell surface with the MUSCL approach of van Leer [12] in conjunction with the *minmod* limiter. Denoting the vector of extrapolated quantities as  $W$ :

$$W_{j+\frac{1}{2}}^R = W_{j+1} - \frac{1}{2} \tilde{\Delta}_{j+\frac{3}{2}} \quad (2.9)$$

$$W_{j+\frac{1}{2}}^L = W_j + \frac{1}{2} \tilde{\Delta}_{j+\frac{1}{2}} \quad (2.10)$$

where:

$$\tilde{\Delta}_{j+\frac{1}{2}} = \text{minmod}(\Delta_{j+\frac{1}{2}}, \Delta_{j-\frac{1}{2}}) \quad (2.11)$$

and  $\Delta_{j+\frac{1}{2}} = W^R - W^L$ . Several choices of  $W$  are possible, e.g., the vector of conserved variables ( $W = U$ ) or characteristic variables. For the present method we choose to extrapolate the primitive variables ( $W = \{\rho, u, v, p\}$ ) and  $U$  is extracted from the extrapolated  $W$ . With the addition of the *minmod* limiter, the algorithm reverts to first order accuracy at shocks in order to preserve monotonicity within the solution.

The formula of Eqn. 2.8 exhibits two major difficulties. First, it may introduce discontinuities in the solution at sonic and stagnation points where the eigenvalues change sign and some form of eigenvalue smoothing may be necessary. A more serious flaw in Eqn. 2.8 is that it introduces excessive numerical damping in the boundary layers. This damping significantly deteriorates

the prediction accuracy of surface quantities of engineering interest. With direct algebraic manipulation of the normal flux near a surface under boundary layer conditions, MacCormack and Candler [6] proved that the Steger Warming procedure introduces artificial tangential momentum exchange between adjacent cells in the boundary layer solely due to the splitting of the inviscid fluxes. This diffusive term is proportional to the quantity:

$$\frac{c}{2\gamma} \rho_{i,j} (u_{i,j+1} - u_{i,j}) \quad (2.12)$$

where  $c$  is the speed of sound and  $\gamma$  is the ratio of specific heats. Since it is of order  $\Delta y$ , it can obtain unacceptably high values in the boundary layer. In addition, there is also a large numerical exchange of kinetic energy of the order:

$$\frac{c}{2\gamma} \rho_{i,j} (\alpha_{i,j+1} - \alpha_{i,j}) \quad (2.13)$$

between adjacent points in the boundary layer where  $\alpha$  is the kinetic energy. They recommended that both  $B_{j+\frac{1}{2}}^+$  and  $B_{j+\frac{1}{2}}^-$  be evaluated at the *same* point. Two choices are obvious: 1) evaluate  $B$  at  $j + \frac{1}{2}$  by averaging the conserved variables between points  $j$  and  $j + 1$ , or 2) evaluate  $B$  at  $j$  and  $j + 1$  respectively in successive iterations. No significant difference is observed between results obtained with either approach. In the present calculations, the first approach is utilized exclusively. The inviscid MacCormack and Candler flux ( $G_{MC}$ ) reads therefore:

$$\begin{aligned} G_{MC,j+\frac{1}{2}} &= B_{j+\frac{1}{2}}^+ U^L + B_{j+\frac{1}{2}}^- U^R \\ &= [S^{-1}C^{-1}|\Lambda^+|CS]_{j+\frac{1}{2}} U^L + [S^{-1}C^{-1}|\Lambda^-|CS]_{j+\frac{1}{2}} U^R \end{aligned} \quad (2.14)$$

where once again,  $U^L$  and  $U^R$  are evaluated with the MUSCL approximation (Eqns 2.9, 2.10 and 2.11). This modification, however, introduces an artificial pressure gradient. This error comprised the terms:

$$\frac{\gamma-1}{2} \rho_{i,j} \left[ (u_{i,j+\frac{1}{2}} - u_{i,j})^2 + (v_{i,j+\frac{1}{2}} - v_{i,j})^2 \right] \quad (2.15)$$

and may, therefore, be expected to dominate only in the close vicinity of the boundary where high velocity gradients exist. MacCormack and Candler [6] treated this problem at the expense

of reintroducing some of the diffusiveness of the original Steger Warming scheme by further modifying the component  $S$  for the matrix  $Q$  in Eqn. 2.7 such that its last row is evaluated as in the original formulation. Subsequently, MacCormack<sup>1</sup> suggested that since this error arises due to the multiplication of the last row of the matrix  $S$  and the column vector  $U$ , this product be explicitly replaced with the extrapolated pressure at the interface. This latter approach is followed in the present computations.

The MC method was developed for application only in the boundary layers and in fact leads to instability when applied in regions of discontinuities such as shock waves. As a result, it is necessary to revert to the original Steger Warming scheme near shocks. This is achieved in a smooth and systematic manner by defining the parameter  $\chi_1$ :

$$\chi_1 = \frac{1}{1 + PR \times PR} \quad (2.16)$$

$$PR = \frac{|p_{i,j+1} - p_{i,j}|}{\min(p_{i,j+1}, p_{i,j})} \quad (2.17)$$

and defining the flux at the  $j + 1/2$  face as:

$$G_{j+\frac{1}{2}} = \chi_1 G_{MC, I_{j+\frac{1}{2}}} + (1 - \chi_1) G_{OSW, I_{j+\frac{1}{2}}} \quad (2.18)$$

## 2.2 van Leer's Flux-Vector Split Algorithm

The functional form of the van Leer scheme [3] is similar to the Steger Warming algorithm. For supersonic flow:

$$G^+ = G; \quad G^- = 0 \quad \text{for } M_y \geq 1 \quad (2.19)$$

$$G^+ = 0; \quad G^- = G \quad \text{for } M_y \leq -1 \quad (2.20)$$

where  $M_y$  is the local Mach number normal to the face  $j + \frac{1}{2}$ . For subsonic flow,  $G$  was revised by van Leer to avoid the discontinuity exhibited across sonic lines by the Steger Warming algorithm.

---

<sup>1</sup>Private Communication, June, 1990

For  $|M_y| < 1$  and  $c$  representing the local speed of sound [17]:

$$G^\pm = \begin{pmatrix} g_{mass}^\pm \\ g_{mass}^\pm u \\ g_{mass}^\pm \frac{(\gamma-1)v \pm 2c}{\gamma} \\ g_{energy}^\pm \end{pmatrix} \quad (2.21)$$

where:

$$g_{mass}^\pm = \pm \frac{\rho c (M_y \pm 1)^2}{4} \quad (2.22)$$

$$g_{energy}^\pm = f_{mass}^\pm \left[ \frac{((\gamma-1)v)^2}{2(\gamma^2-1)} + \frac{u^2}{2} \right] \quad (2.23)$$

This scheme also obtains second order accuracy with the MUSCL approach (Eqns. 2.9 through 2.11).

## 2.3 Roe's Flux-Difference Split Algorithm

The formula for this scheme reads [13]:

$$G_{j+\frac{1}{2}} = \frac{1}{2} \left[ G(U_{j+\frac{1}{2}}^L) + G(U_{j+\frac{1}{2}}^R) \right] - \frac{1}{2} \hat{R}_{j+\frac{1}{2}} |\hat{\Lambda}_{j+\frac{1}{2}}| \hat{R}_{j+\frac{1}{2}}^{-1} (U_{j+\frac{1}{2}}^R - U_{j+\frac{1}{2}}^L) \quad (2.24)$$

where  $(\cdot)$  indicates evaluation at the Roe averaged state between  $U^L$  and  $U^R$  [13]. This scheme extends to second order accuracy through the MUSCL approach (Eqns. 2.9 and 2.10) with  $W = \{\rho, u, v, p\}$ . In contrast to the above flux vector split algorithms, Roe's scheme may violate the entropy condition when the eigenvalues at the Roe averaged state vanish. Following Harten [41] the eigenvalues  $|\lambda|$  of  $|A|$  are modified when they are below some small threshold  $\delta$ :

$$|\lambda| = \frac{|\lambda^2 + \delta^2|}{2\delta} \quad |\lambda| < \delta \quad (2.25)$$

where the value of  $\delta$  is taken as the following [10]:

$$\delta = \tilde{\delta} J^{-1} \left[ |\vec{u} \cdot \vec{\nabla} \xi| + |\vec{u} \cdot \vec{\nabla} \eta| + \frac{c}{2} (|\vec{\nabla} \xi| + |\vec{\nabla} \eta|) \right] \quad (2.26)$$

The value of  $\tilde{\delta}$  utilized typically in the range 0.05 to 0.1. For the flow past the compression ramp, only the two eigenvalues of the form  $u + c$  and  $u - c$  (corresponding to the genuinely nonlinear eigenvectors) are cutoff in each direction. For blunt body flows, however, it is necessary also to apply the cutoff algorithm to the eigenvalue of the form  $u$  (corresponding to the linearly degenerate eigenvector) in the streamwise (body-tangential or  $\xi$ ) direction for stability purposes [42]. Further, the value of the cutoff parameter,  $\tilde{\delta}$  also needs to be increased to prevent the development of anomalous solutions as discussed later. This can however lead to excessive dissipation. To prevent this for both the blunt body and the corner flow, an anisotropic cutoff formula described by Muller [43] is employed in the streamwise  $\xi$  direction:

$$\delta = \tilde{\delta} J^{-1} \lambda^{(\xi)} \left[ 1 + \left( \frac{\lambda^{(\eta)}}{\lambda^{(\xi)}} \right)^{\frac{2}{3}} \right] \quad (2.27)$$

where  $\lambda^{(k)} = |\vec{u} \cdot \vec{\nabla} k| + c |\vec{\nabla} k|$ . Further discussion on the choice of the parameter  $\tilde{\delta}$  is provided with the results.

### 3. Boundary Conditions and Numerical Details

For each flow, the boundaries may be categorized into one of the following:

- “Inflow/Farfield boundary:” The flow vector  $\{\rho, \rho u, \rho v, \rho e\}$  is specified corresponding to the known values.
- Solid boundary: The velocity vector and the normal pressure gradient are assumed zero and a fixed surface temperature is specified i.e.:

$$\rho \vec{v} = 0; \quad T = T_w; \quad \frac{\partial p}{\partial n} = 0 \quad (3.1)$$

where  $\vec{v}$  is the velocity vector and the subscript  $w$  refers to wall conditions. The values of  $T_w$  are provided with the results.

- Outflow boundaries: The flow at these boundaries is assumed predominantly supersonic. The zero gradient extrapolation condition ( $\partial/\partial \xi = 0$ ) is applied.

The boundary conditions for the implicit portion of the algorithm are described in Gaitonde and Shang [16].

Convergence is determined for all computations by monitoring several quantities. The global residual, defined as:

$$\|G.R.\| = \frac{1}{(IL)(JL)} \sqrt{\sum_{i=1}^{IL} \sum_{j=1}^{JL} \sum_{k=1}^4 \left( \frac{R_k}{\hat{U}_\infty} \right)^2} \quad (3.2)$$

is one measure. In Eqn. 3.2,  $k$  denotes the  $k^{th}$  equation (1=continuity, 2,3=momentum and 4=energy) on an  $IL \times JL$  computational mesh and  $R_k$  is the residual:

$$R_k \cong \frac{\partial \hat{U}_k}{\partial t} = -\frac{\partial \hat{F}_k}{\partial \xi} - \frac{\partial \hat{G}_k}{\partial \eta} \quad (3.3)$$

For plotting purposes, these values are normalized by the value of  $\|G.R.\|$  obtained after the first iteration. With this criterion, convergence is assumed after  $\|G.R.\|$  drops 8 or more orders of magnitude. After this, the surface pressure and heat transfer are monitored over about one

characteristic time ( $T_c = L/U_\infty$  where  $U_\infty$  is the freestream velocity and  $L$  is a macroscopic length scale, the diameter of the cylinder for the blunt body flow or the length from the leading edge to the corner for the corner flow). In addition, the integrated root mean square (RMS) pressure and heat transfer values over the entire surface are also monitored. Both must remain constant at convergence. With  $p$  denoting pressure the RMS surface pressure may be written as:

$$RMSP = \frac{1}{IL} \sqrt{\sum_{i=1}^{IL} \left( \frac{p_{i,j=surface}}{p_\infty} \right)^2} \quad (3.4)$$

With  $Q$  denoting surface heat transfer, the RMS Surface Heat transfer is:

$$RMSQ = \frac{1}{IL} \sqrt{\sum_{i=1}^{IL} (Q_{i,j=surface})^2} \quad (3.5)$$

## 4. Blunt Body Flow

### 4.1 Flow Parameters and Grid Details

The parameters for this flow are:

$$\begin{aligned}M_{\infty} &= 16.34 \\ \text{Cylinder Radius} &= 1.5 \text{ in} \\ T_{\infty} &= 93.93R \\ p_{\infty} &= 0.01203\text{psia} \\ \text{Reynolds Number} &= 1.2 \times 10^6 \text{ per foot} \\ T_{\text{wall}} &= 530R\end{aligned}$$

This case represents a low-enthalpy flow for which previous computations validate the perfect gas approximation [44]). Three grids (denoted 1, 2 and 3 respectively) are developed with the characteristics described in Table 4.1. In this table, the number of flow points listed in each direction,  $IL \times JL$ , do not include shadow cells employed on the boundary. Guidelines for grid resolution are taken from the work of Klopfer and Yee [45] who recommend a surface cell Reynolds number ( $Re_c$ ) of roughly 3 for heat transfer calculations (fixed-wall temperature) and of the order of 10 for adiabatic wall conditions for their TVD scheme. They also indicate that heat transfer rates are not particularly sensitive to the circumferential spacing. The most refined grid for each computation satisfies these criteria and is generated with a combination of exponentially stretched and uniform spacings (Fig. 2(a)). From this complete grid, subgrids 1 and 2 are extracted systematically to provide grid refinement studies. Note that the surface cell Reynolds numbers presented in Table 4.1 are based on the half-cell heights of the first cell on the body.



Table 4.1: Blunt body grid details

Grid	$IL \times JL$	$Re_c _{min}$	$Re_c _{max}$	$Re_c _{av}$	$\Delta\theta _{min}$	$\Delta\theta _{max}$	$\Delta\theta _{av}$	$c _{av}$
1	$19 \times 17$	19.4	125.3	51.5	1.10	10.5	6.6	1.98
2	$39 \times 35$	8.1	51.6	20.6	0.51	5.3	3.4	1.41
3	$79 \times 71$	3.7	24.2	9.6	0.25	2.5	1.7	1.18

Legend:  $IL$  - Points in  $\xi$  direction  $JL$  - Points in  $\eta$  direction  
 $Re_c$  - Surface mesh Reynolds number  $\Delta\theta$  - Angular spacing (deg)  
 $c$  - Stretch factor at surface

Subscripts:  $av$  - average  $min$  - minimum  
 $max$  - maximum

## 4.2 Results

Computations with each of the methods are compared with experimental values published by Holden *et al.* [46]. Results from the MC scheme are displayed in Fig. 3 where the unnormalized computed surface pressure is plotted versus  $\theta$ , the angle measured in degrees along the cylinder with reference to the stagnation streamline,  $\theta = 0$ . Not much variation with mesh resolution is observed in the quantitative pressure results. The experimental measured pressure values display significant scatter and are consistently lower than the computations. A similar observation was made by Prabhu *et al.*. The computed stagnation point pressure compares very well with the results obtained with the Rayleigh supersonic pitot pressure formula [47], 4.20psia, and the computed results of Prabhu *et al.* [44]. Fig. 4 shows the unnormalized computed heat transfer (in  $Btu/f^2s$ ) versus  $\theta$ . Overall, the agreement with the experimental values is excellent even with the coarsest mesh computed which has a very high surface cell Reynolds number (Table 4.1). The stagnation heat transfer agrees very well with the Fay and Riddell value (as quoted by Prabhu *et al.*) of 49.5  $Btu/f^2s$ . It should be noted that the MC method, proposed as a correction to the

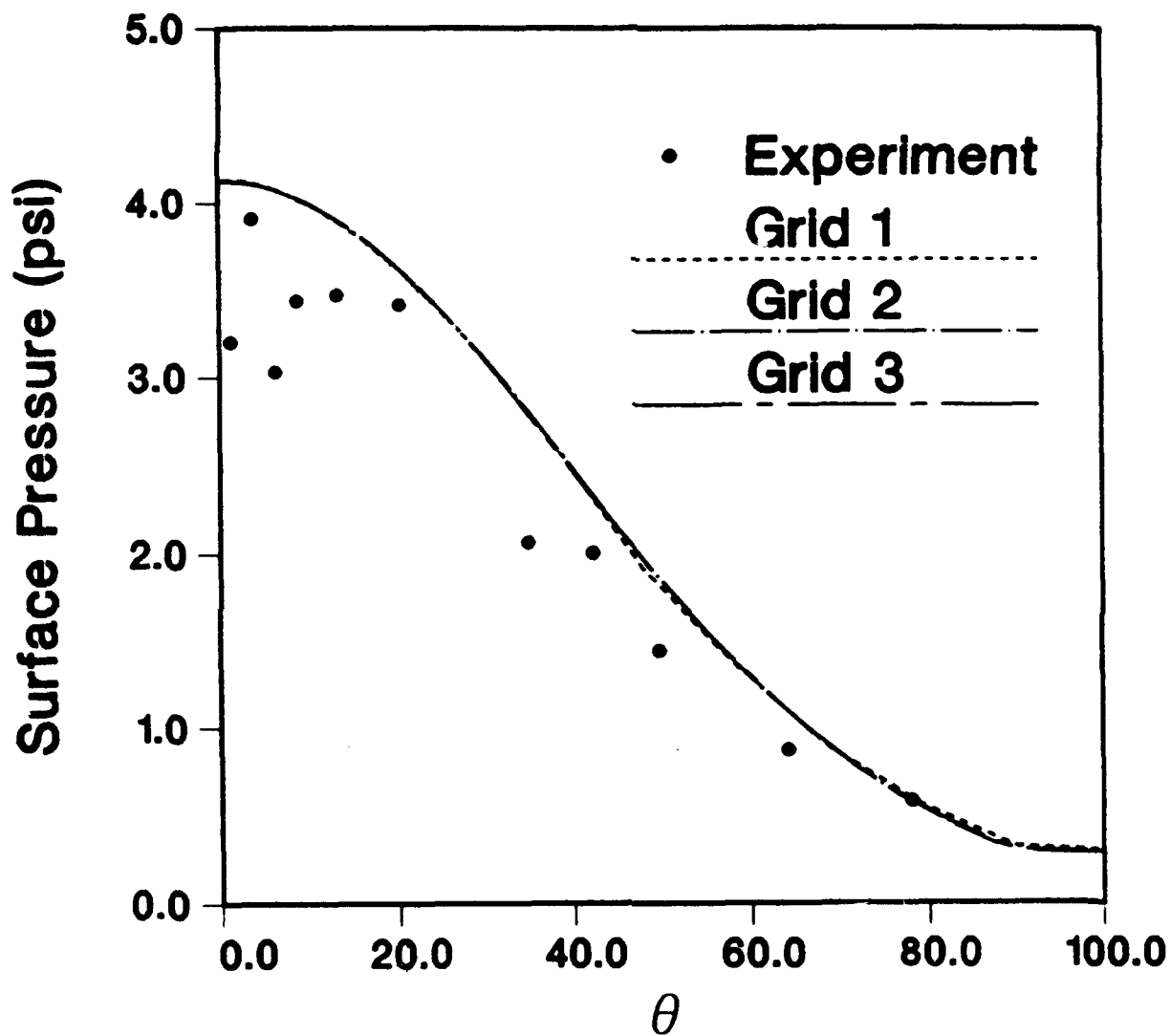


Figure 3: Surface pressure in Mach 16 flow past a blunt body with the MC scheme

original Steger Warming (OSW) method, is a tremendous improvement. Results from the OSW method (not shown for the purposes of brevity) indicate an overprediction of heat transfer of 500%, 400% and 250%, respectively, over the Fay and Riddell value on Grids 1, 2 and 3 respectively.

One drawback of the MC algorithm over the OSW algorithm is the tendency to develop the anomalous "carbuncle" solutions referred to earlier. The OSW algorithm does not display any such tendency for the grids computed. Since the MC algorithm is supposed to revert to the OSW method at shocks, this is more appropriately characterized as a drawback of the switching algorithm utilized in the present research. Indeed, for the results displayed here, the carbuncle problem was eliminated by explicitly applying the OSW scheme at a few points on either side of the shock, i.e., overriding the pressure-based switching mechanism described earlier. Fig. 5 exhibits the Mach number variation versus distance (measured relative to the cylinder center) and normalized by the cylinder radius along the stagnation streamline. For each mesh, the shock is captured with at most two points inside. The shock standoff distance, defined with reference to the location of the sonic point, is uniform with mesh resolution ( $\Delta/R \sim 0.4$ ). These results are in close agreement with the results of Prabhu *et al.* and reflect well upon the shock capture capability of the OSW method.

For the sake of completeness, we show the computed Mach, pressure and temperature contours in Fig. 6. With the strategy of explicit application of the OSW scheme in the vicinity of the shock, no evidence of the carbuncle is visible.

Fig. 7 shows the surface pressure prediction with the van Leer method. As for the MC results, the pressure prediction does not change much with grid resolution and, in fact the pressure over the entire surface of the cylinder differs only by an insignificant amount from that predicted by the MC method. In sharp contrast, grid resolution has a drastic effect upon the heat transfer prediction (Fig. 8). Although all the heat transfer profiles are smooth, results on the coarse mesh overpredict the heat transfer by a large amount over the entire surface of the cylinder (120% over the Fay and Riddell value at the stagnation point). The results improve significantly with grid resolution with 52% overprediction of stagnation heat transfer on Grid 2 and a relatively small 15% overprediction on Grid 3. These results indicate the extreme diffusiveness of the van Leer scheme,

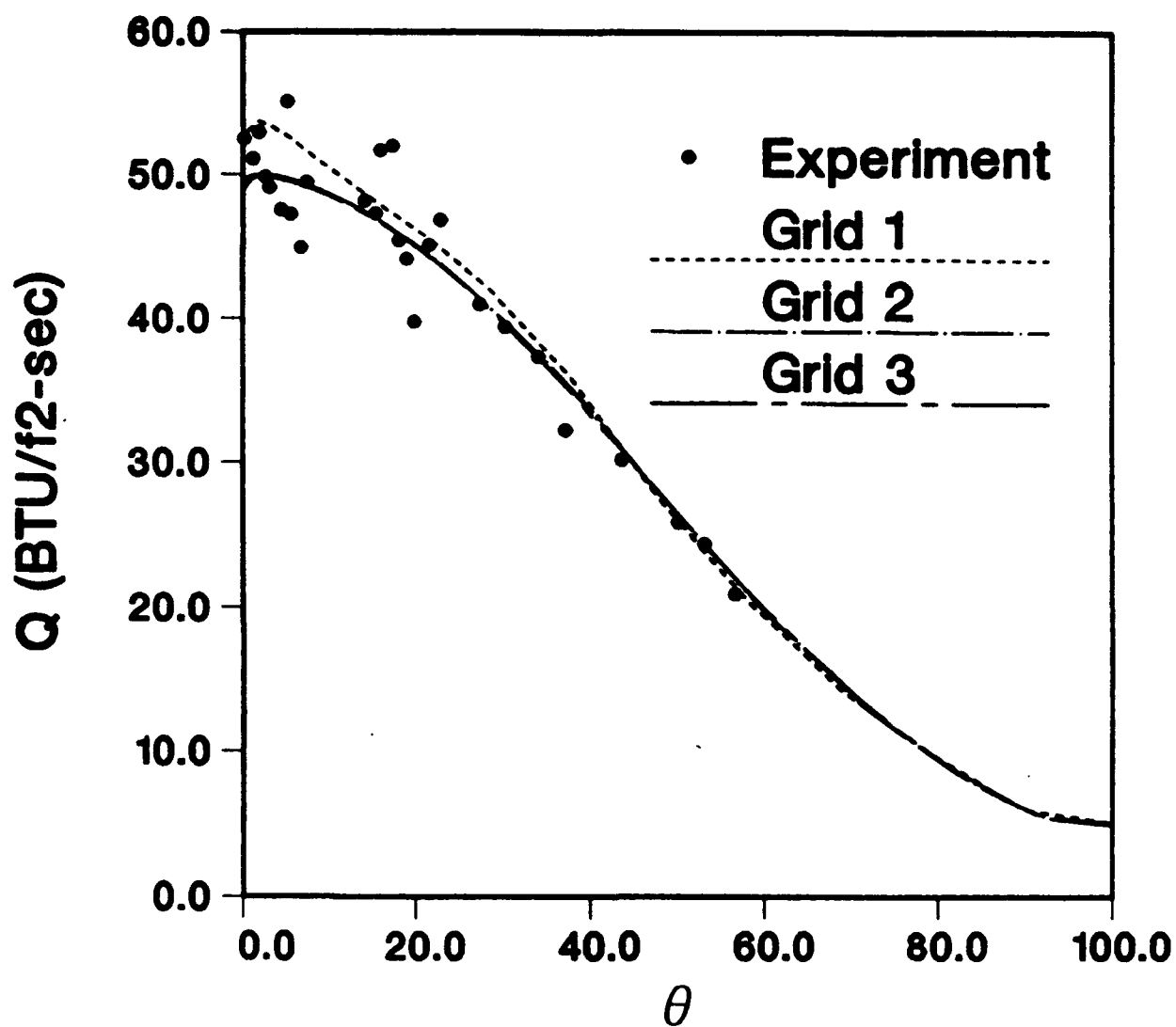


Figure 4: Heat transfer in Mach 16 flow past a blunt body with the MC scheme

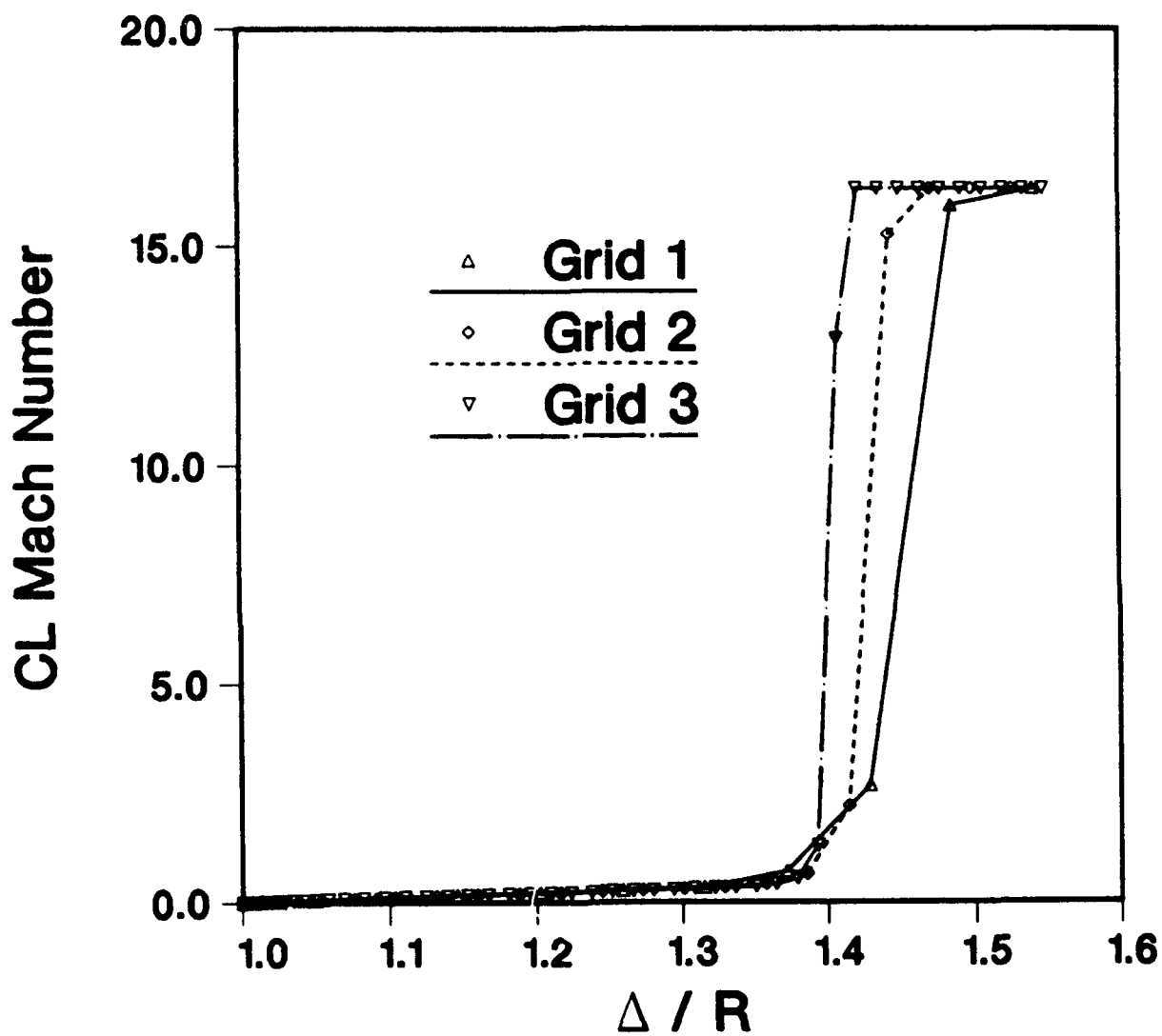


Figure 5: Mach number along stagnation streamline for Mach 16 flow past a blunt body with the MC scheme

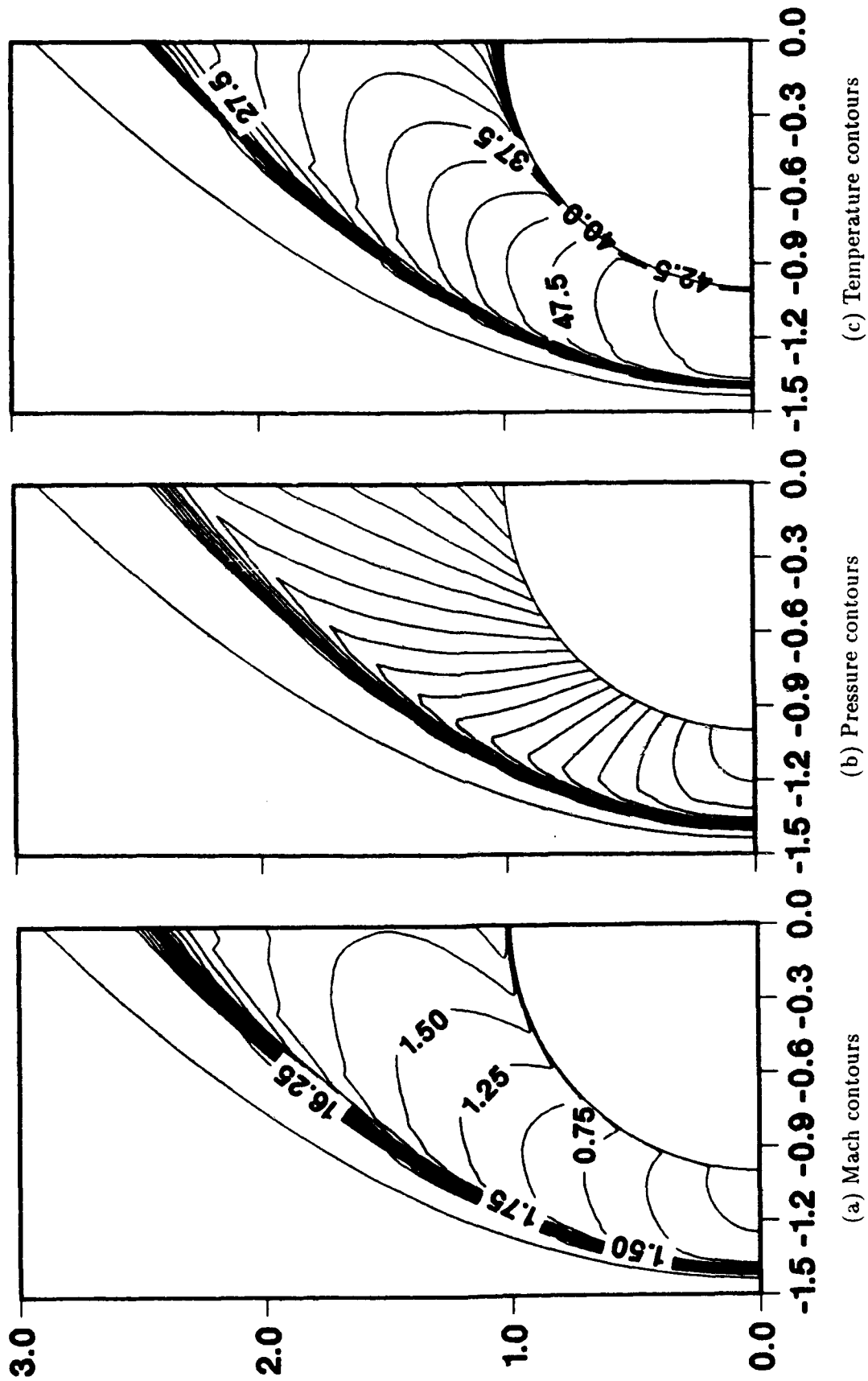


Figure 6: Contours for blunt body flow with the MC scheme

a result previously observed by other researchers on other geometries and flow parameters [22]. Despite the significant inaccuracies in the heat transfer prediction, the method exhibits excellent shock-capture capability (Fig. 9). For all mesh resolutions, the shock is not only captured within two zones along the centerline but also, the shock standoff for each grid is within one grid point. It is noted that none of these calculations with van Leer's scheme tended to exhibit any tendency towards the development of the anomalous "carbuncle" solution. The computed Mach, pressure and temperature contours are presented in Fig. 10.

An attempt was made to improve the predictions of heat transfer by investigating different choices of the extrapolated vector  $W$  (see Section 2). As mentioned earlier, all of the calculations described in this work utilize  $W = \{\rho, u, v, p\}$  for the extrapolation procedure to obtain the  $L$  and  $R$  states. The effect of utilizing  $W = \{\rho, \rho u, \rho v, p\}$  and the set of conserved variables  $W = \{\rho, \rho u, \rho v, \rho e\}$  was investigated for the van Leer scheme on Grid 2. It was found that neither of these had any significant influence on the accuracy of the final result (Fig. 11) and, in fact, the rate of convergence was found to be adversely affected.

Turning to the Roe scheme (Fig. 12), once again the computation of the surface pressure displays a remarkable insensitivity to grid resolution. This is perhaps a result of the fact that the surface pressure is a mechanical quantity, dictated mainly by the shock strength and shape which in turn is rather accurately predicted by all the inviscid discretization methods at each level of mesh refinement. In this regard, the fact that the mesh is well aligned with the shock wave is an important factor. For Grids 2 and 3, several values of the cutoff parameter  $\tilde{\delta}$  were utilized for reasons outlined below. The effect of this parameter on the computed surface pressure is clearly negligible.

Fig. 13 exhibits the surface heat transfer comparison with experiment. For Grid 1, the value of  $\tilde{\delta}$  used was quite small (0.05). No tendency toward the development of the carbuncle was observed and the results are quite accurate in similarity with the predictions with the MC scheme. As mentioned previously, Roe's scheme exhibits a tendency to display the carbuncle for this configuration as observed previously by Peery *et al.* [31] and Liou *et al.* [33]. In the present instance, this tendency is suppressed by increasing the value of the constant  $\tilde{\delta}$  in the entropy

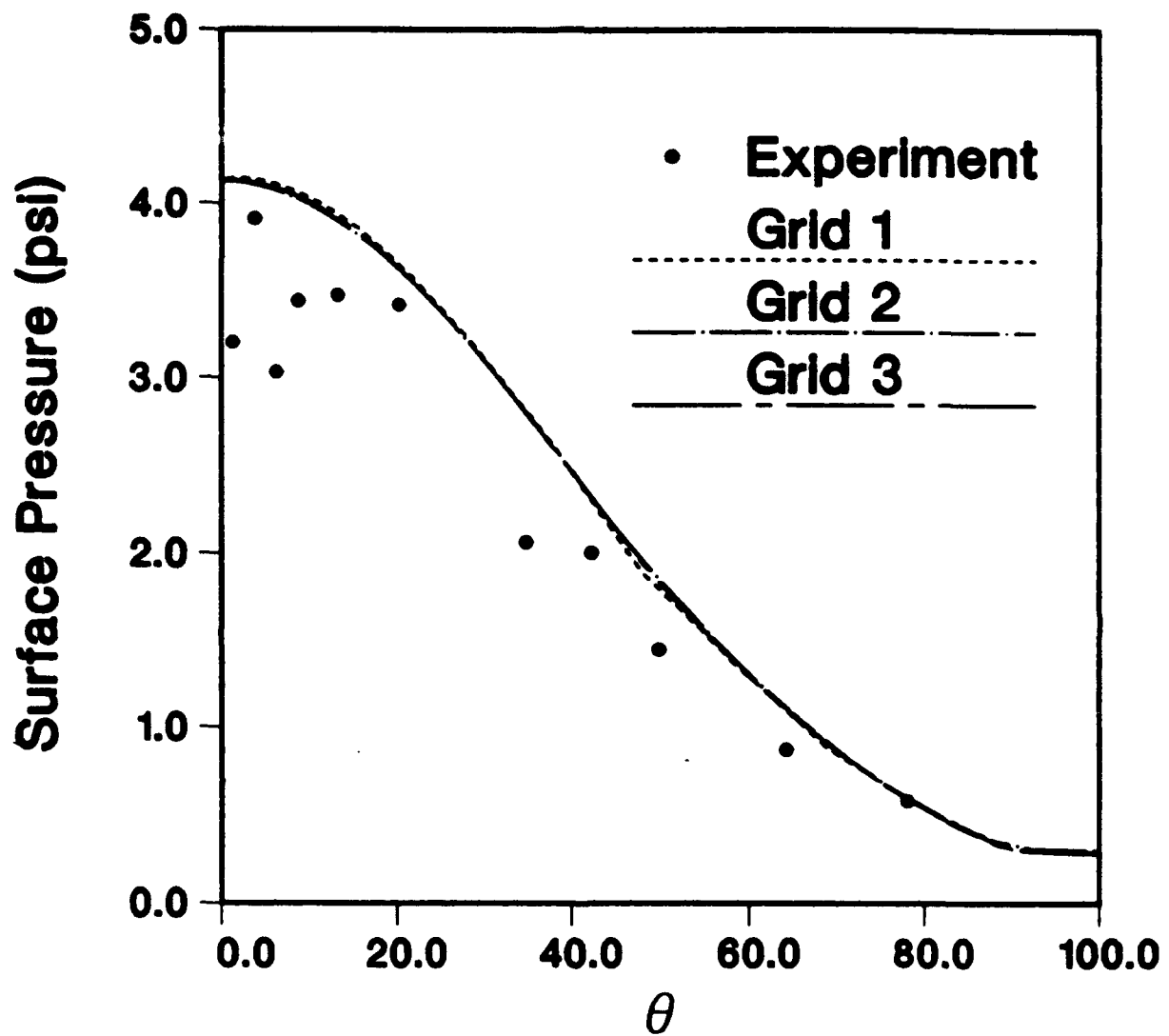


Figure 7: Surface pressure in Mach 16 flow past a blunt body with the van Leer scheme



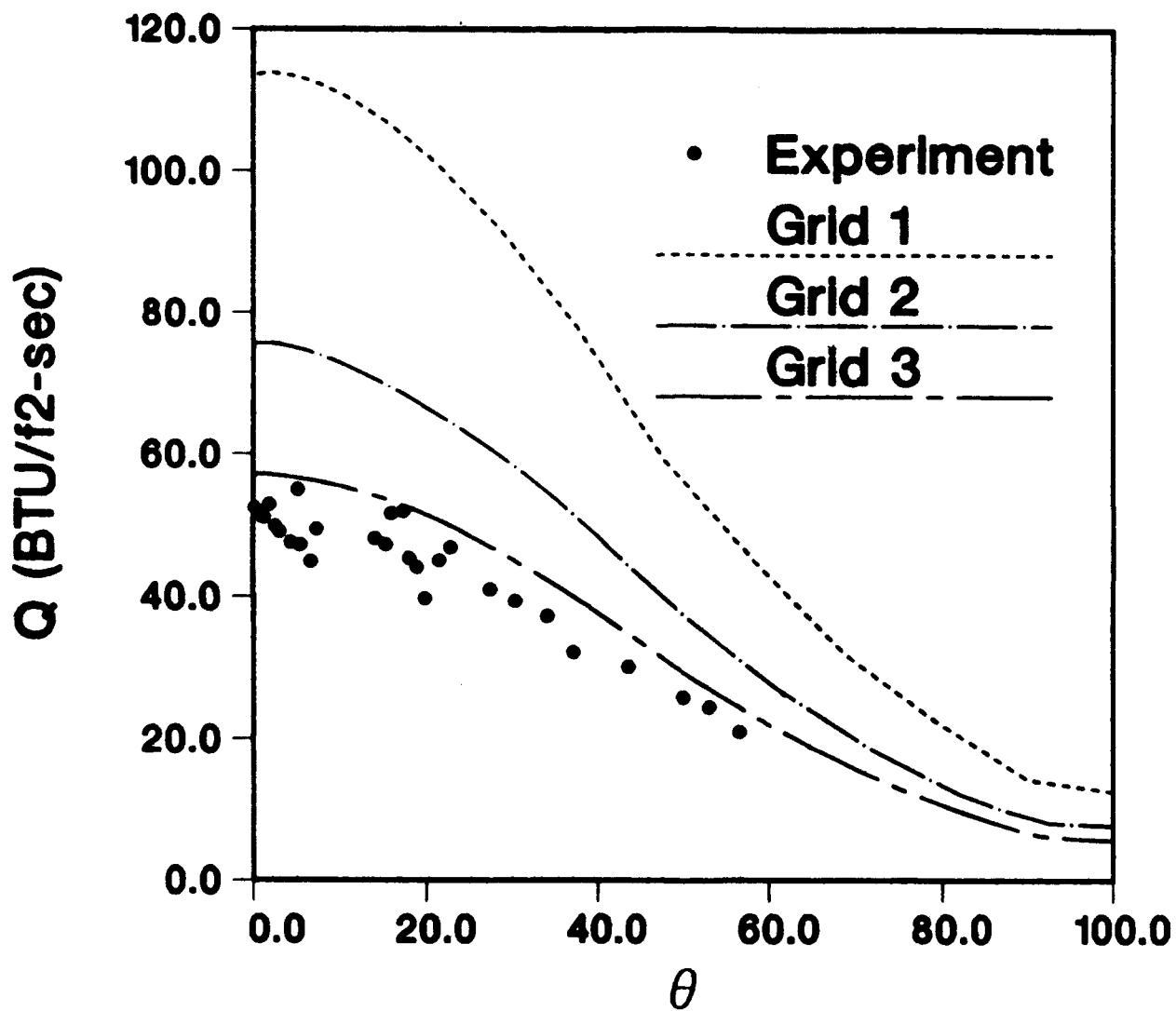


Figure 8: Heat transfer in Mach 16 flow past a blunt body with the van Leer scheme

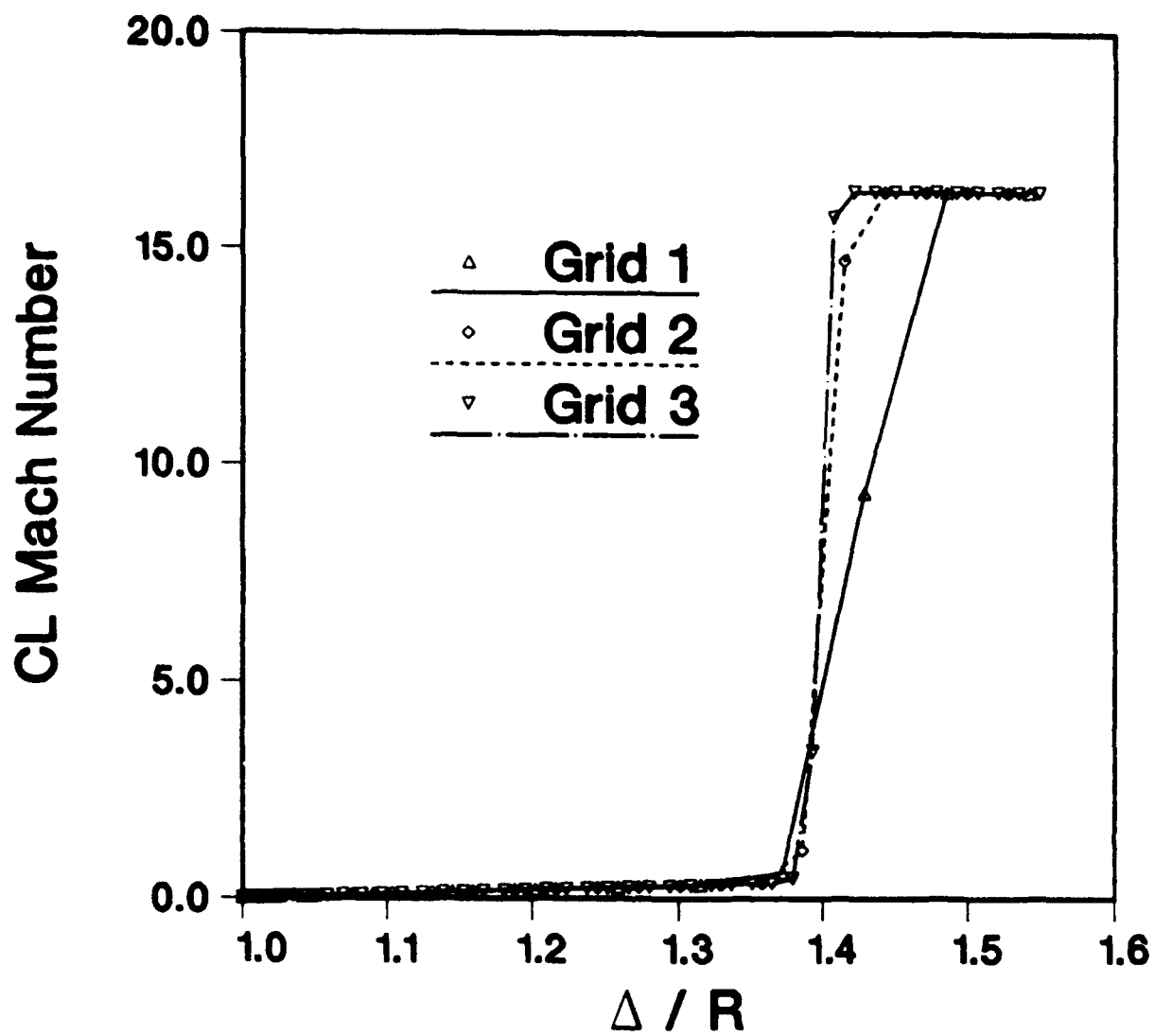


Figure 9: Mach number along stagnation streamline for Mach 16 flow past a blunt body with the van Leer scheme

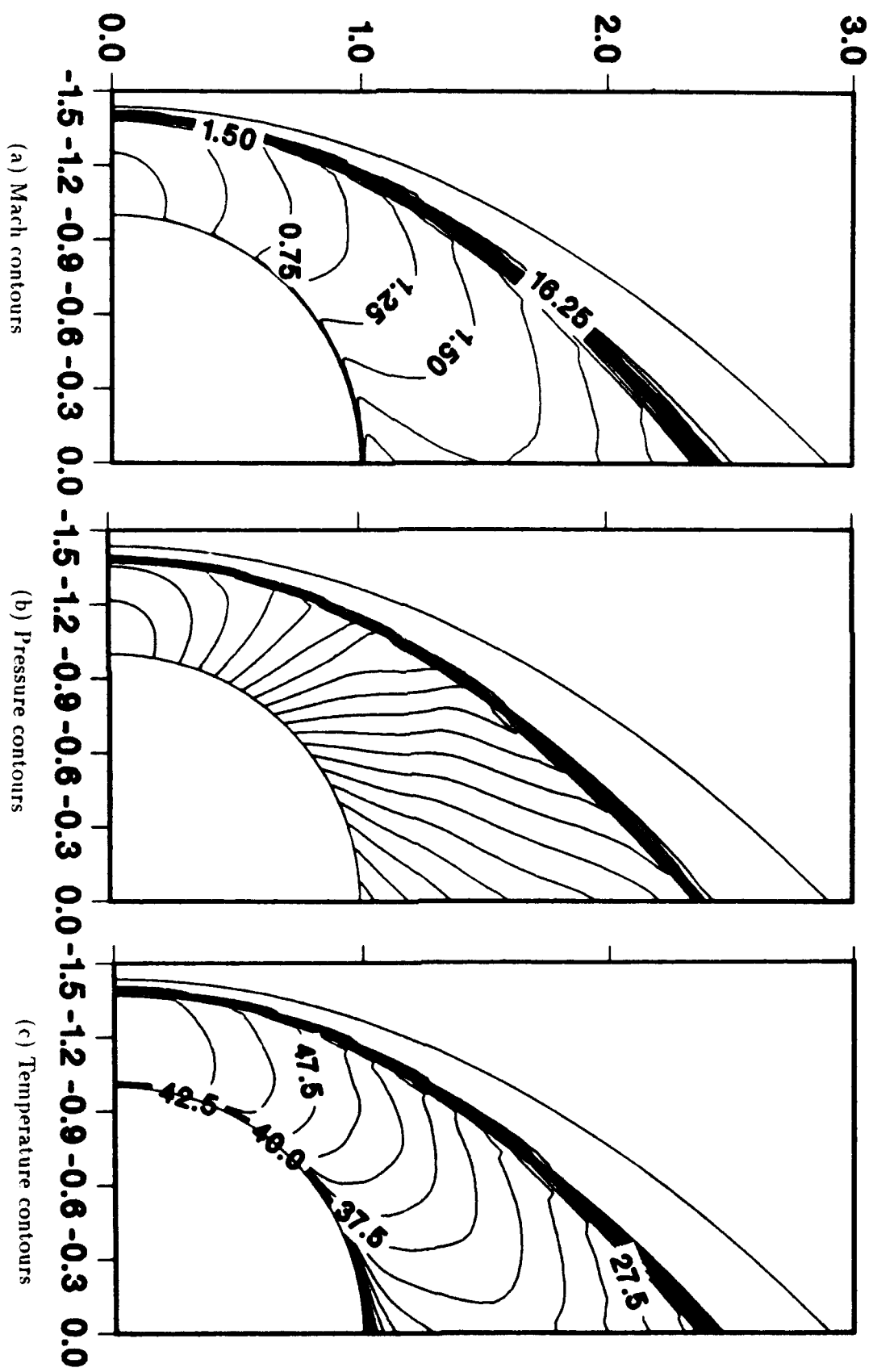
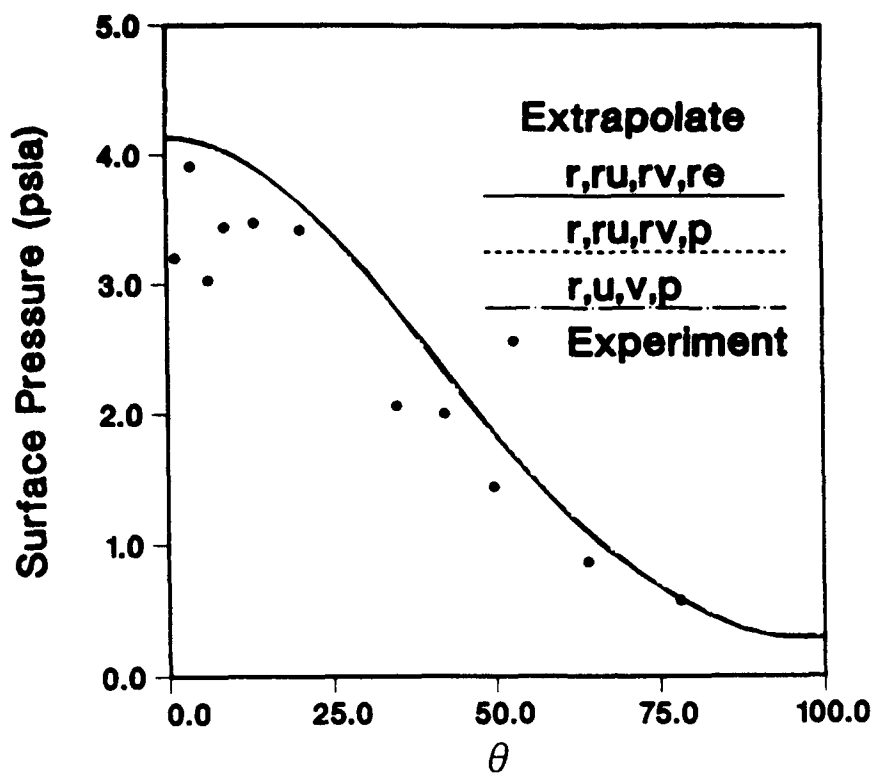
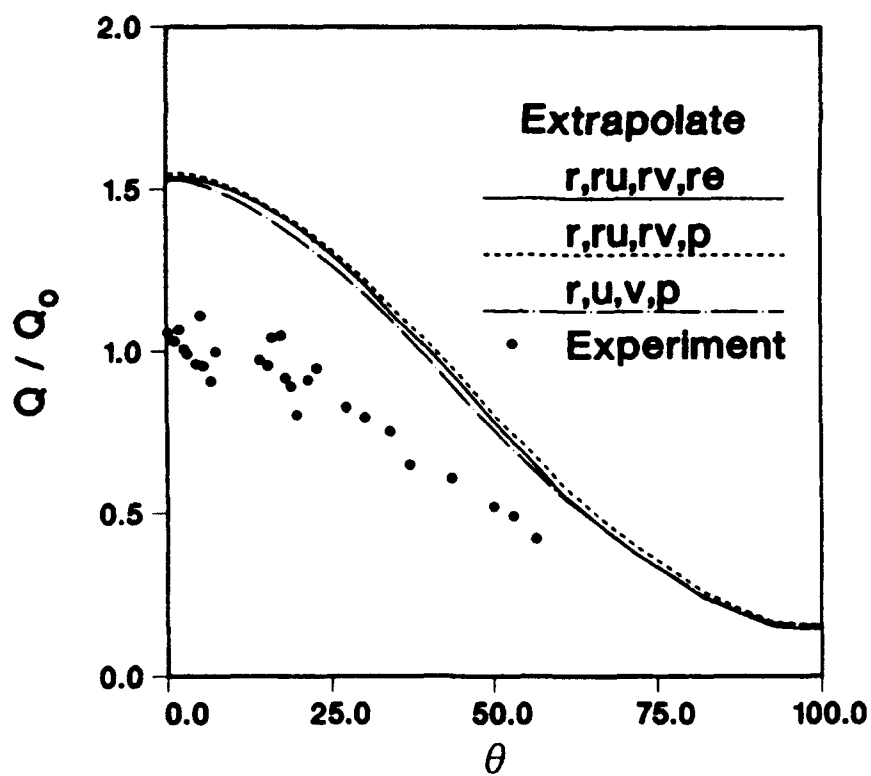


Figure 10: (c) contours for blunt body flow with the van Leer scheme



(a) Surface pressure



(b) Surface heat transfer

Figure 11: Effect of extrapolation of different variables on surface quantities with the van Leer scheme

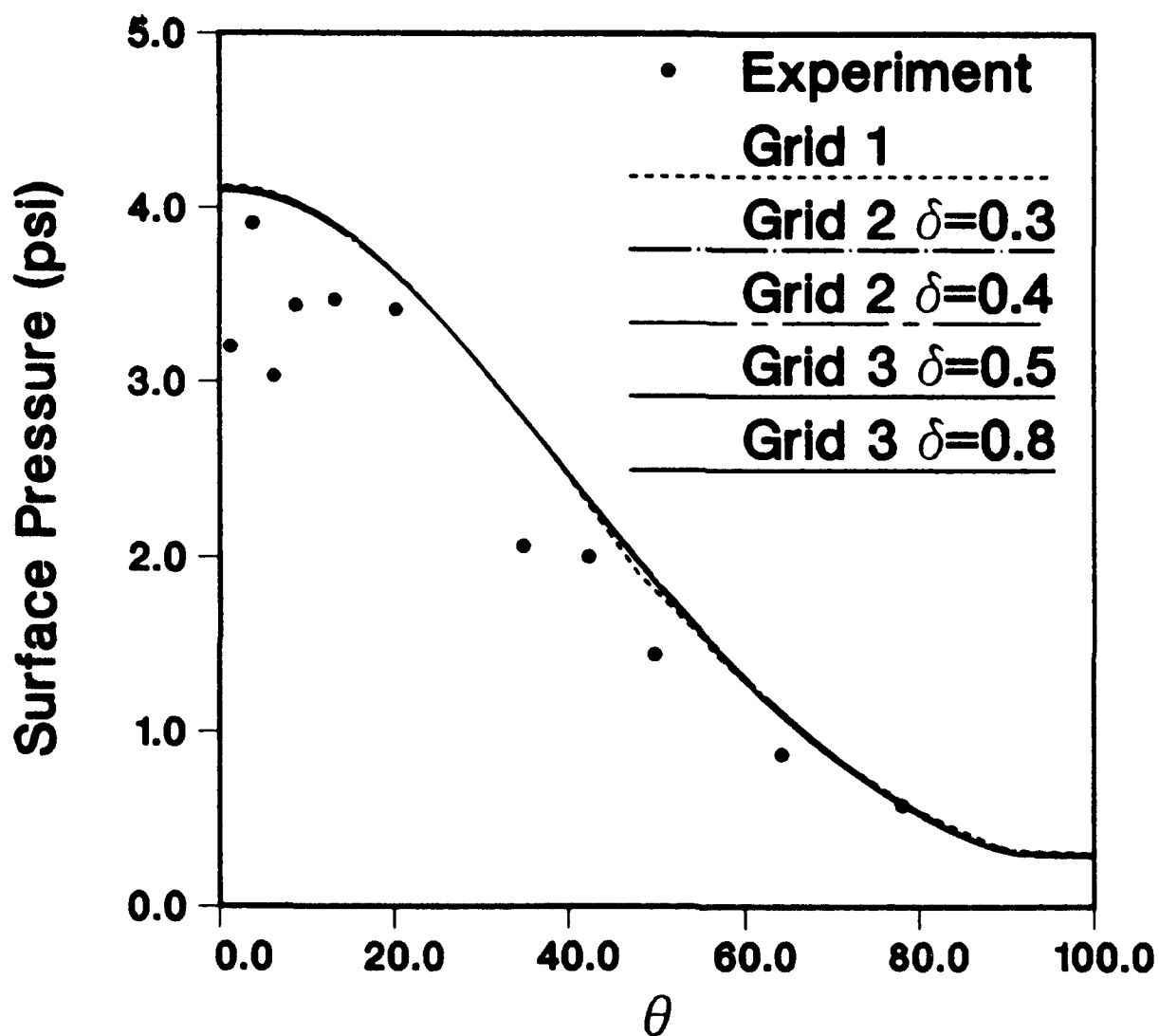


Figure 12: Surface pressure in Mach 16 flow past a blunt body with the Roe scheme

correction formula (Eqns. 2.26 and 2.27). For Grid 1, we believe the truncation error provided by the coarseness of the mesh is possibly sufficient. For Grid 2, small values tended to give the bulge solution clearly visible in the Mach contours. At about  $\tilde{\delta} = 0.2$ , the visible evidence of the bulge in the Mach contours disappeared. However, a small dip remained in the surface quantities of interest in the vicinity of the stagnation point. Upon increasing  $\tilde{\delta}$  to 0.3, all evidence of the carbuncle disappeared. As shown in Fig. 13, further increase to 0.4 did not have any significant effect upon the flowfield. Although a rigorous examination of the minimum value allowable for an anomaly free solution was not made, for Grid 3, the value of  $\tilde{\delta}$  was increased in increments of 0.1 until all evidence of anomaly in contour plots of the Mach number, pressure and temperature disappeared. A minimum value of 0.5 was required. Even then, a small dip persisted in the heat transfer computation in the vicinity of the stagnation point (Fig. 13). Further increase upto  $\tilde{\delta} = 0.8$  did not remove this anomaly. The shock standoff distance and shock capture capability (Fig. 14) are similar to that exhibited by the van Leer scheme. In general, the shock is captured within at most two points even with the highest value of  $\tilde{\delta}$  utilized. The computed flowfield exhibits no evidence of the carbuncle in the flow contours (Fig. 15). Further, the standoff distance (roughly 40% of the radius) is quite accurate and invariant with grid resolution. On all schemes considered, this reflects very well upon the computed density ratio across the bow shock and overall low conservation errors.

The excellent agreement observed for heat transfer results with the MC and Roe scheme may be fortuitous. Further numerical studies are necessary at different Mach and Reynolds number conditions to validate the conclusions derived in the previous discussion.

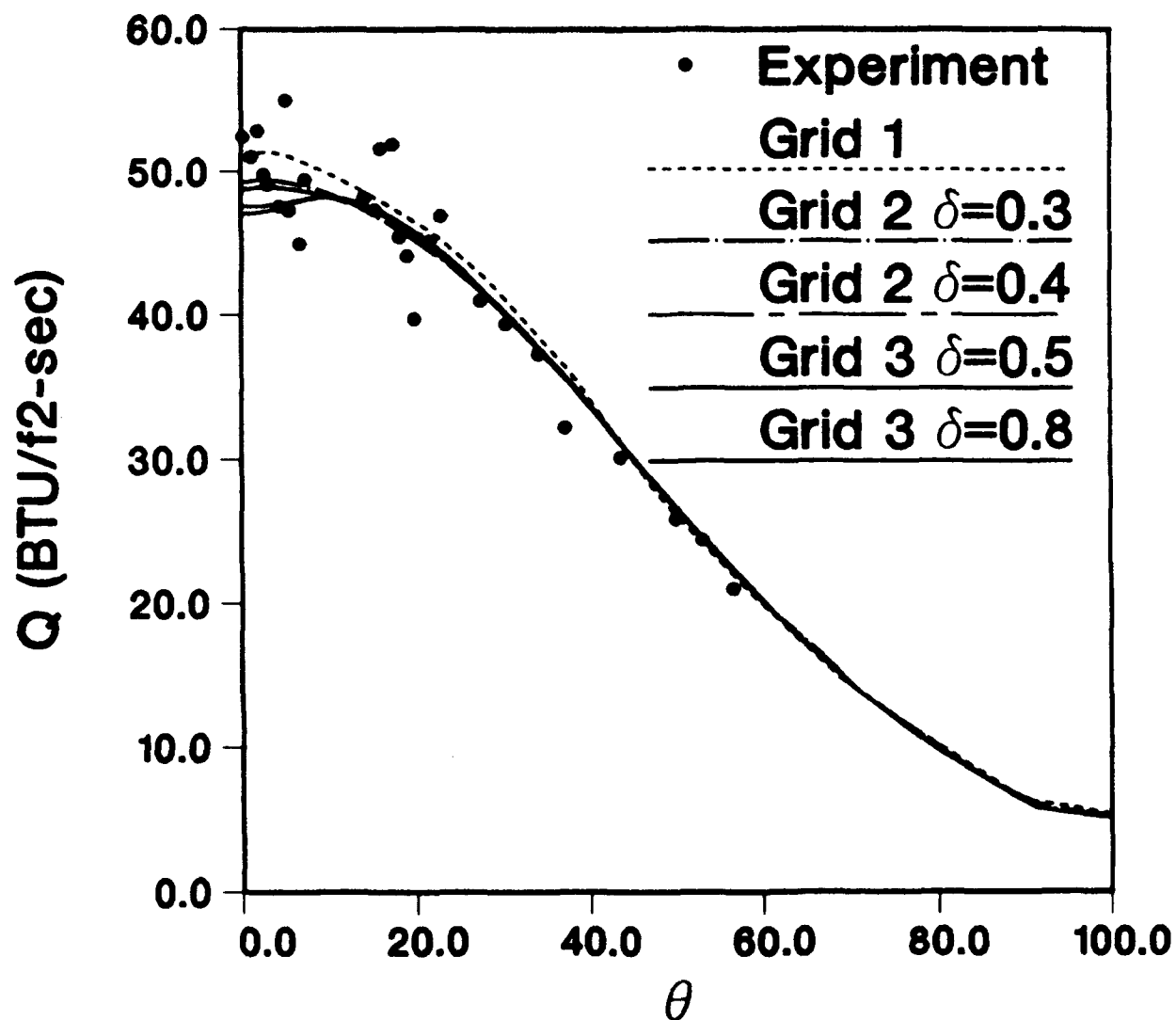


Figure 13: Heat transfer in Mach 16 flow past a blunt body with the Roe scheme

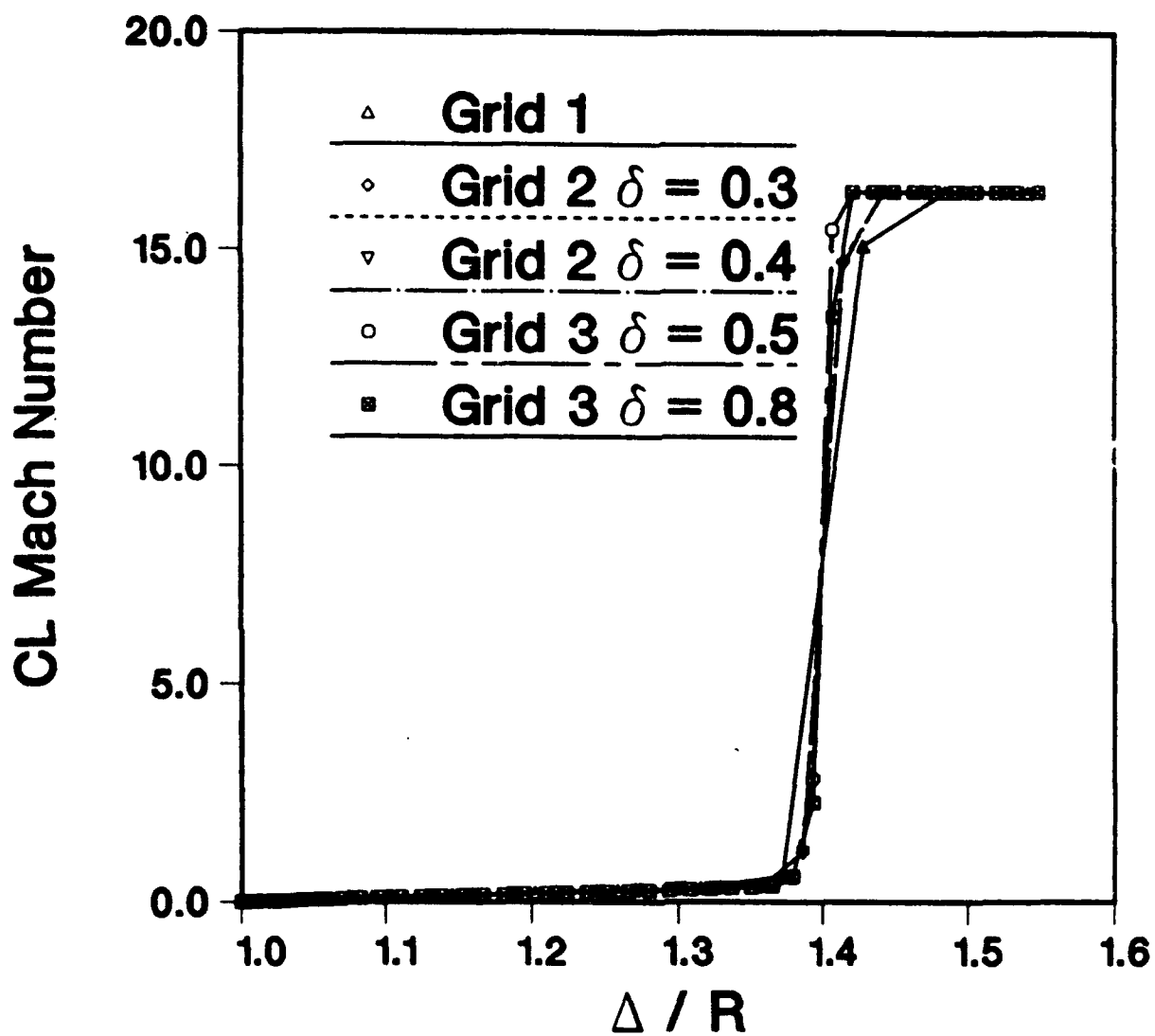


Figure 14: Mach number along stagnation streamline for Mach 16 flow past a blunt body with the Roe scheme



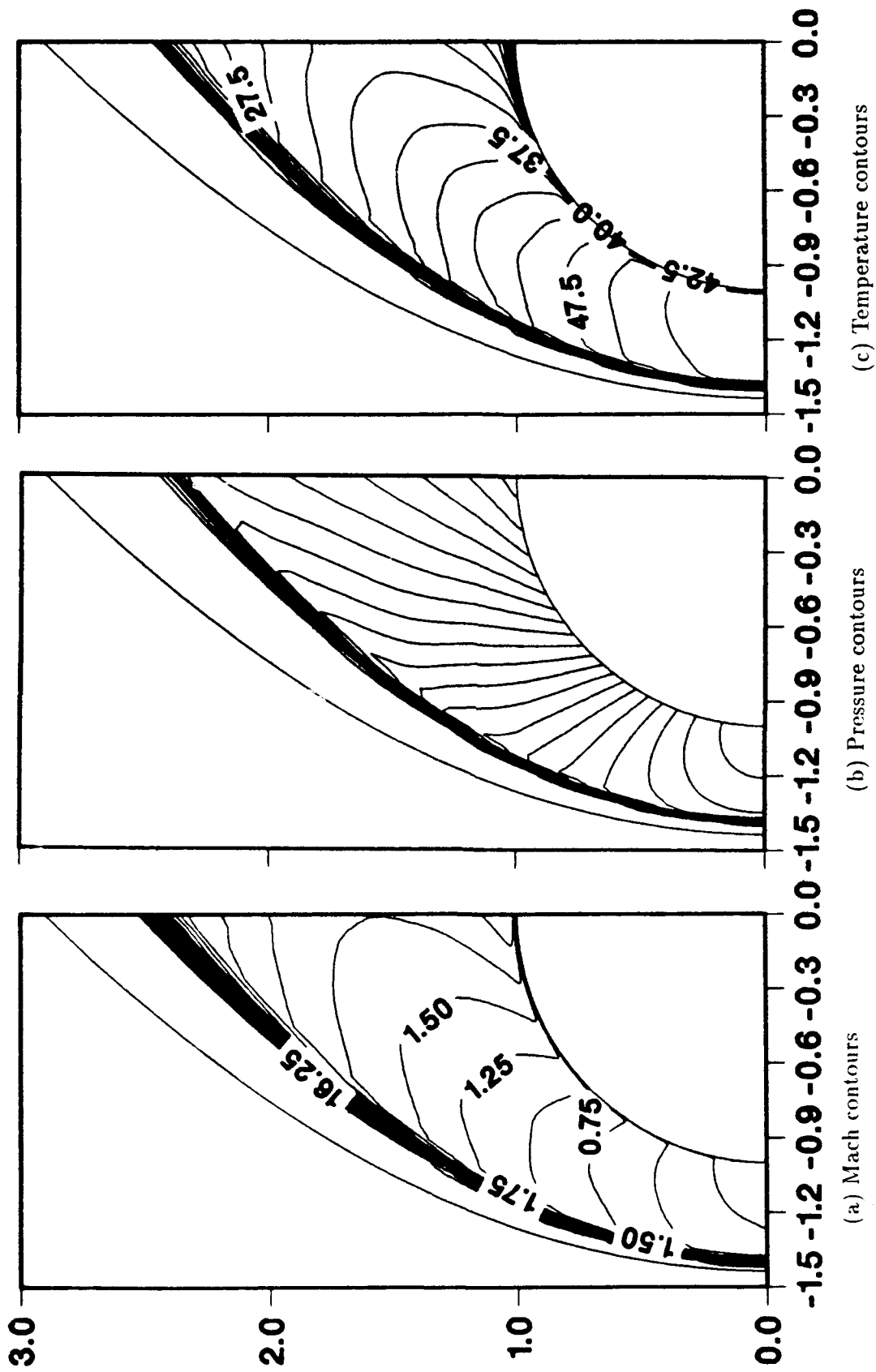


Figure 15: Contours for blunt body flow with the Roe scheme

## 5. Corner Flow

### 5.1 Flow Parameters and Grid Details

The parameters for this flow, chosen to simulate the experimental evidence of Holden *et al.* [34]), are:

$$\begin{aligned}M_{\infty} &= 14.1 \\ \text{Ramp Angle} &= 24^{\circ} \\ T_{\infty} &= 130.8R \\ p_{\infty} &= 0.21 \\ \text{Reynolds Number} &= 72000 \text{ per foot} \\ T_{\text{wall}} &= 535R\end{aligned}$$

Two types of grid are considered for this study, Grids 1, 2 and 3 are simply sheared (Fig. 2(b1)) exponentially stretched on either side of the interaction and also in the surface normal direction. Since recent research efforts have highlighted the importance of resolving the leading edge shock [36], Grid 4 utilizes  $209 \times 59$  points providing better resolution in the vertical direction at the leading edge by suitable redefinition of the domain at the leading edge (Fig. 2(b2)). The horizontal spacing over the solid surface is the same as for Grid 3. The characteristics of the grids utilized are presented in Table 5.1.

### 5.2 Results

Fig. 16 (a), (b) and (c) display the comparison of pressure coefficient (defined as  $2 \frac{p_w - p_{\infty}}{\rho_{\infty} u_{\infty}^2}$ ) with the MC, van Leer and Roe schemes, respectively. The abscissa is the streamwise distance normalized by the distance from the leading edge to the corner ( $L = 1.44 ft$ ). On the coarse mesh, all methods predict the start of pressure rise at an  $X/L$  value of 1.0, significantly upstream of the

Table 5.1: Corner grid details

Grid	$IL \times JL$	$Re_c _{av}$	$\Delta x _{min}$	$\Delta x _{max}$	$\Delta x _{av}$	$c _{av}$
A	$49 \times 14$	47.6	0.02	0.12	0.04	1.4
B	$99 \times 29$	21.7	0.01	0.06	0.02	1.2
C	$199 \times 59$	10.3	0.005	0.03	0.01	1.1
D	$209 \times 59$	5.9	0.005	0.03	0.01	1.1

Legend:  $IL$  - Points in  $\xi$  direction  $JL$  - Points in  $\eta$  direction  
 $Re_c$  - Surface mesh Reynolds number  $\Delta x$  - Streamwise spacing (ft)  
 $c$  - Stretch factor at surface

Subscripts:  $av$  - average  $min$  - minimum  
 $max$  - maximum

experimental value. Further, the peak pressure location as well as magnitude are also considerably underpredicted. For Grid 2, once again, no significant differences between the methods are observed in the pressure coefficient prediction though some improvement is observed of the peak pressure (underpredicted roughly 22%) as well as the initial pressure rise over that obtained on Grid 1. In contrast to Grids 1 and 2 where not much difference is observed between the schemes, the pressure coefficient on Grid 3 displays significant differences between the methods. The initial pressure rise occurring at about  $x/L \sim 0.6$  is best reproduced by the MC method while for the Roe and van Leer schemes, this rise occurs slightly downstream ( $x/L \sim 0.75$ ). The location of the peak pressure is also best captured with the MC method although the magnitude is overpredicted about 12%. On the other hand, the location of the computed peak with the Roe and van Leer schemes is slightly upstream of the experimental value though the magnitude is correctly predicted. There is not much difference in the computed pressure coefficients with Grid 4 over Grid 3 for both the MC and Roe schemes. However, the peak  $C_p$  with van Leer's scheme drops somewhat (3%). All schemes predict the theoretical inviscid pressure rise beyond  $x/L \sim 2$  on

every grid.

The heat transfer results are displayed in Fig. 17 (a), (b) and (c) for the MC, van Leer and Roe schemes, respectively. The ordinate in this figure is the heat transfer coefficient defined as  $k \left( \frac{\partial T}{\partial n} \right)_w / \rho_\infty u_\infty (H_o - H_w)$  where  $H$  is the total enthalpy and the subscript  $w$  denotes evaluation at the wall. The inaccuracies on the coarsest mesh may be predominantly attributed to inadequate grid resolution which leads to significant truncation error. For Grid 2, both the MC method and Roe's method display higher peak heat transfer rates while van Leer's method exhibits a lower peak, each method approaching closer to experimental values relative to Grid 1. On the finest mesh, once again, the MC method predicts the initial drop (corresponding actually to the point of separation as evident later) at the correct location while the Roe and van Leer schemes underpredict upstream influence. On the other hand, the peak value is best predicted with Roe's scheme (15% overprediction) with the MC method overpredicting the heat transfer coefficient the most (30% overprediction). In a manner similar to that observed previously for the pressure coefficient, there is no improvement with Grid 4 over Grid 3. Note that with Roe's scheme, a small dip is observed at  $X/L \sim 1.25$  on Grids 1 and 2, the cause of which is presently unknown. However, with grid refinement, this anomaly is eliminated.

Fig. 18 compares the prediction of the skin friction coefficient, defined as  $2\mu_w \left( \frac{\partial u}{\partial n} \right)_w / \rho_\infty u_\infty^2$ . The size of the separated reverse flow region is indicated by the region of negative  $C_f$ . This increases with grid refinement for all methods. On Grids 1 and 2, once again the MC and Roe schemes yield similar results and van Leer's method overpredicting significantly the peak skin friction. All methods predict almost negligible separation on Grid 1 indicating a lack of adequate resolution of the viscous terms. For the denser Grids (3 and 4), the predictions with van Leer algorithm rapidly approach those with the other two schemes, a trend also observed earlier with the heat transfer. The MC method predicts the most accurate start of the separation region in comparison with experimental values. All three methods, however, fail to correctly locate the trough in skin friction coefficient, most likely due to reattachment, at  $X/L \sim 1.25$ .

Overall, the effect of grid resolution on all methods is to provide better comparison between theory and experiment as anticipated. For the sake of completeness, the computed Mach contours

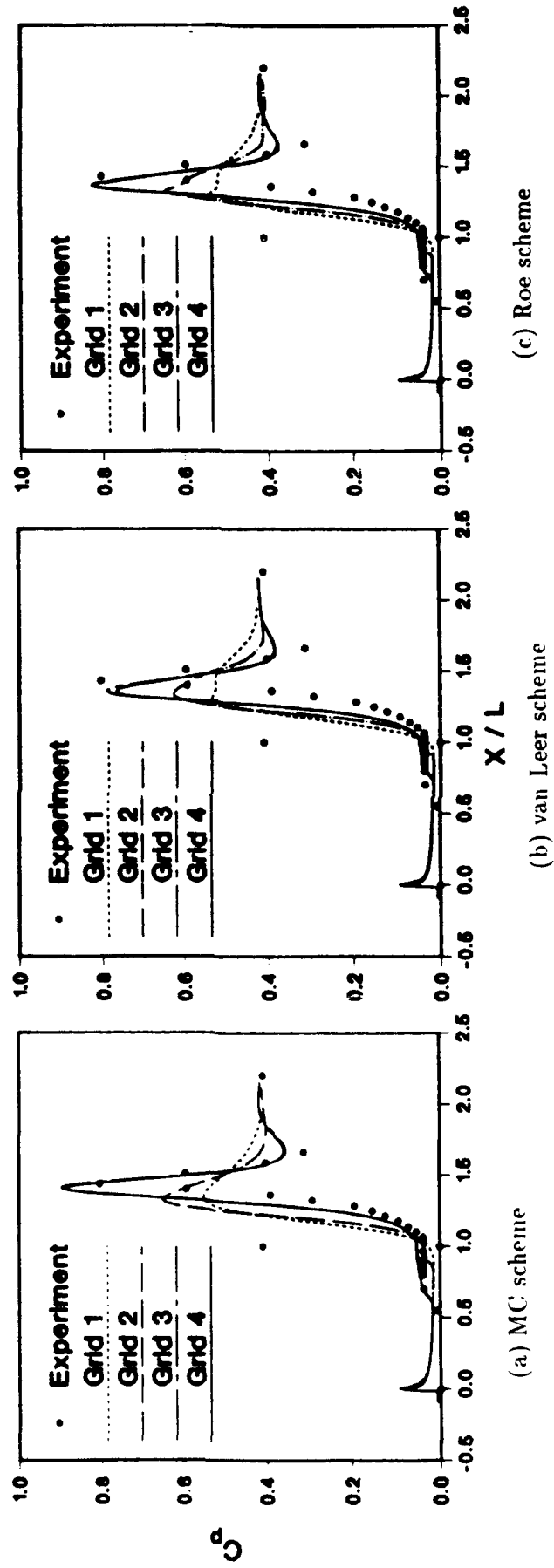
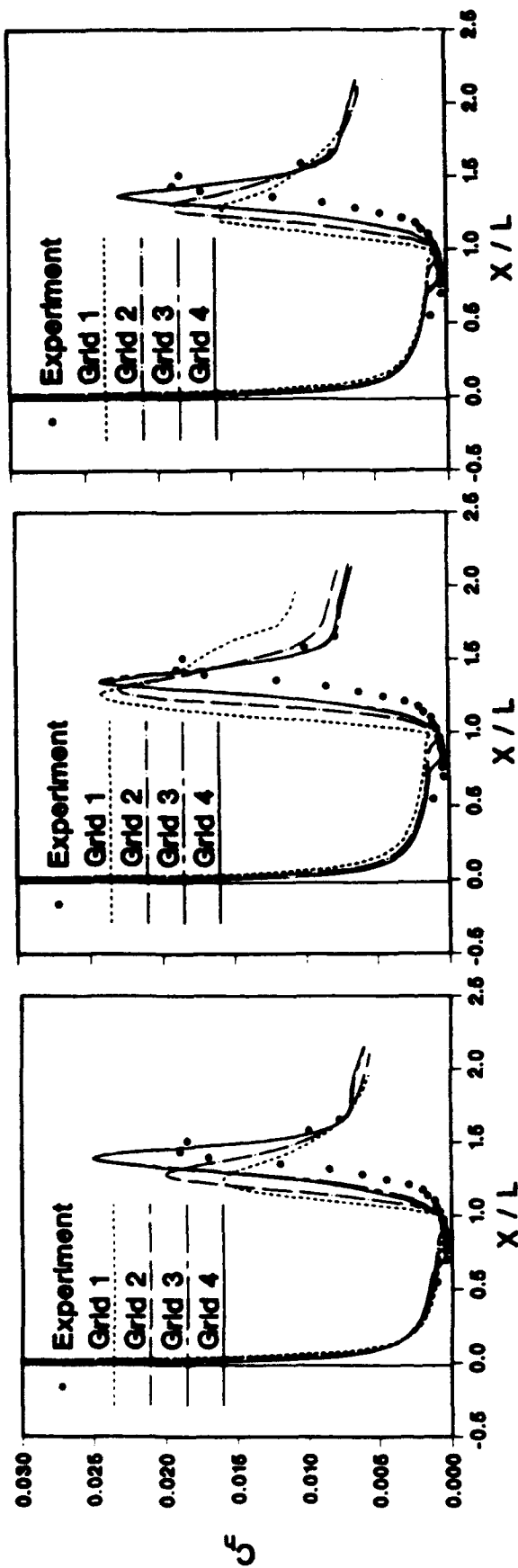


Figure 16: Comparison of pressure coefficient for compression corner flow



(a) MC scheme

(b) van Leer scheme

(c) Roe scheme

Figure 17: Comparison of heat transfer coefficient for compression corner flow

on Grid 4 with each method are presented in Fig. 19. The overall pattern is the same for all methods and similar to that observed on Grid 3 (not shown). The leading edge shock is captured accurately but tends to get smeared near the point where it intersects the corner shock. The resolution of the flow at this point of intersection may be critical for the purposes of accuracy. It is interesting to note that although van Leer's algorithm performs poorly on the coarse mesh, significant improvement is obtained with grid refinement sepecially in the prediction of surface quantities. The salient difference between Meshes 3 and 4 is in the vertical spacing. However, the horizontal spacing is identical except upstream of the leading edge of the plate where Grid 4 has 10 uniformly spaced points. Clearly the issue of horizontal spacing has not been resolved and possibly even better comparison may be obtained with each method if the regions around the points of separation and reattachment are further resolved.

It may be mentioned that the present results on Grids 3 and 4 agree in an overall sense with the computations of other researchers. Although precise comparisons are not possible due to different implementations and mesh details, some differences in trends may be outlined. The CFL3D code (utilizing Roe's scheme with third order approximation and the thin layer equations for the viscous terms) has been utilized for the same configuration by Rudy *et al.* [36] as well as by Rizzetta *et al.* [35]. The results of the former indicate surprisingly good agreement with experimental data on a relatively coarse mesh ( $51 \times 51$ ) though the predictions deteriorate somewhat with higher grid resolution. Their grid independent results (obtained on a  $101 \times 101$  mesh) exhibits a larger separation region than that observed experimentally. However, they note that their time-accurate calculations require about 12ms for steady state to be achieved, 8ms more than observed experimentally and 2ms more than the total experimental time. Indeed, their best comparison with experimental results is obtained during the transients (between 2 and 3ms) in time-accurate computations. In comparison, with the convergence criteria outlined earlier, the results displayed on the Mesh 4 represent a minimum flow development time of 9.5ms for van Leer's scheme - the relevant numbers for the MC scheme and Roe's scheme are 19ms and 17ms, respectively. One difference in trends is that the present methods all display pressure and heat transfer peaks upstream of the experimentally observed location in contrast to those obtained

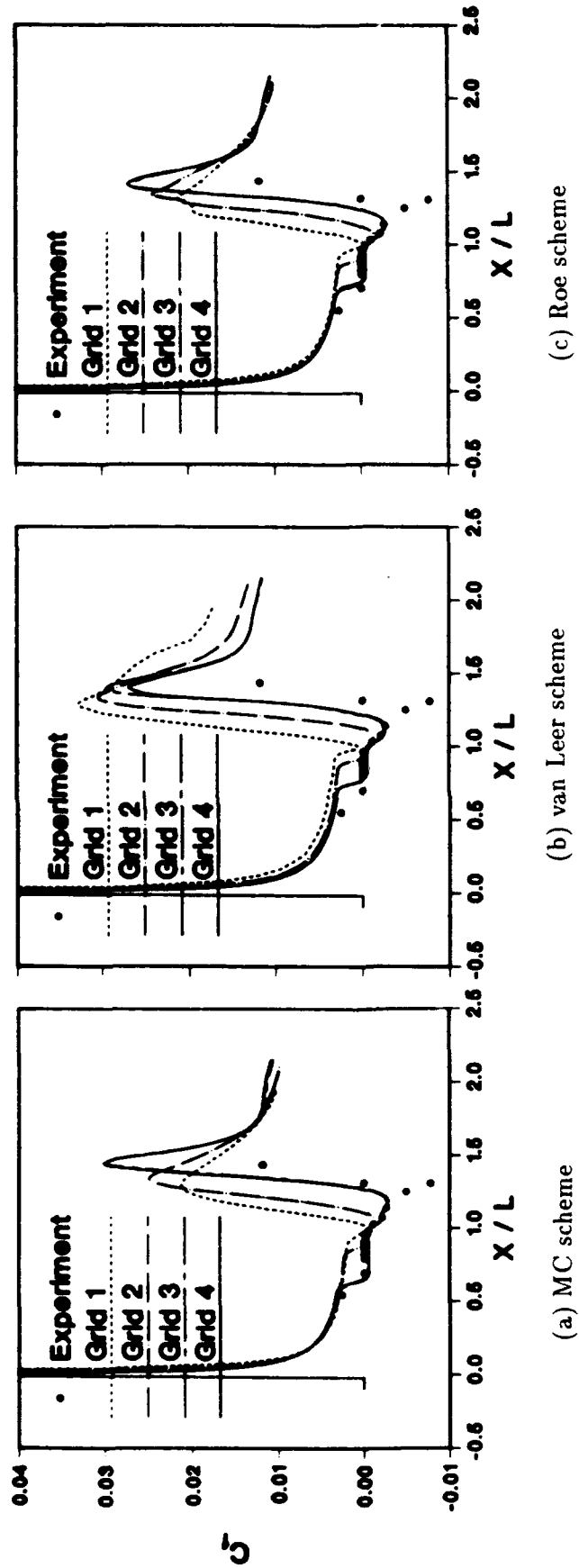
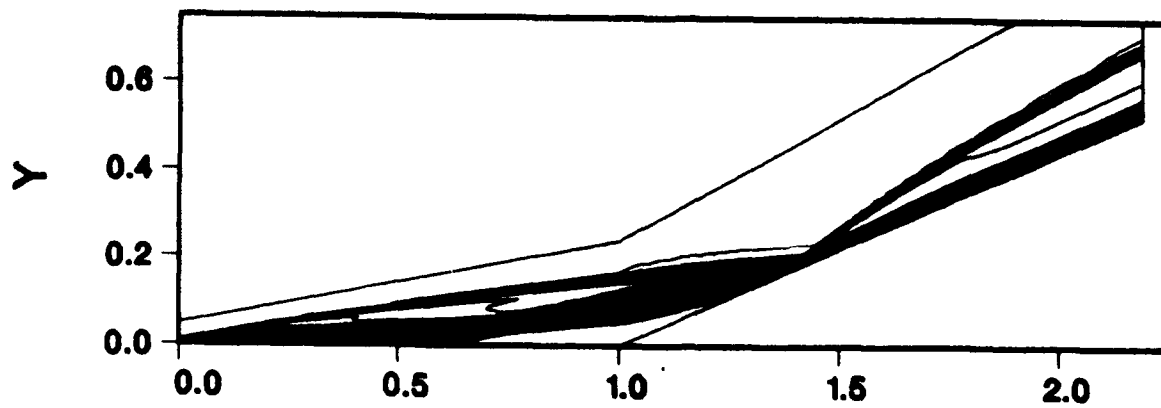


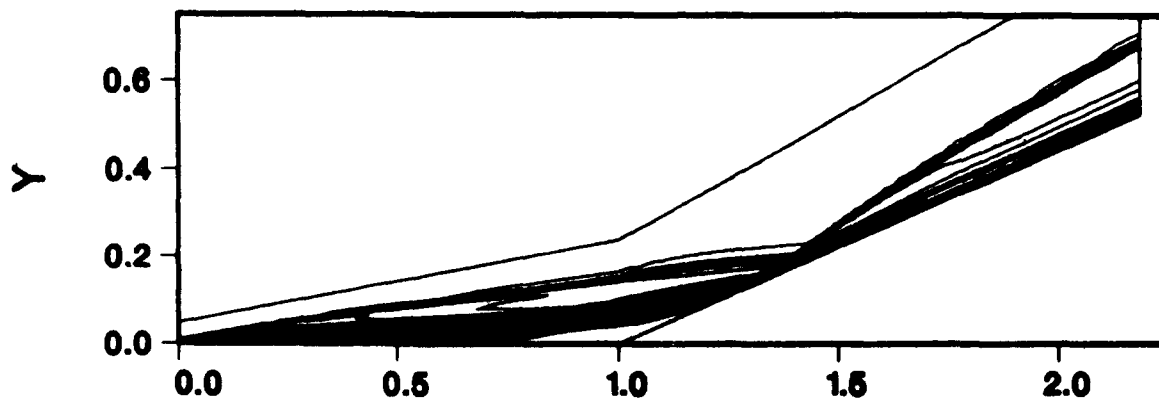
Figure 18: Comparison of skin friction coefficient for compression corner flow



### Corner flow (Grid 4) - MC



### Corner flow (Grid 4) - vL



### Corner flow (Grid 4) - Roe

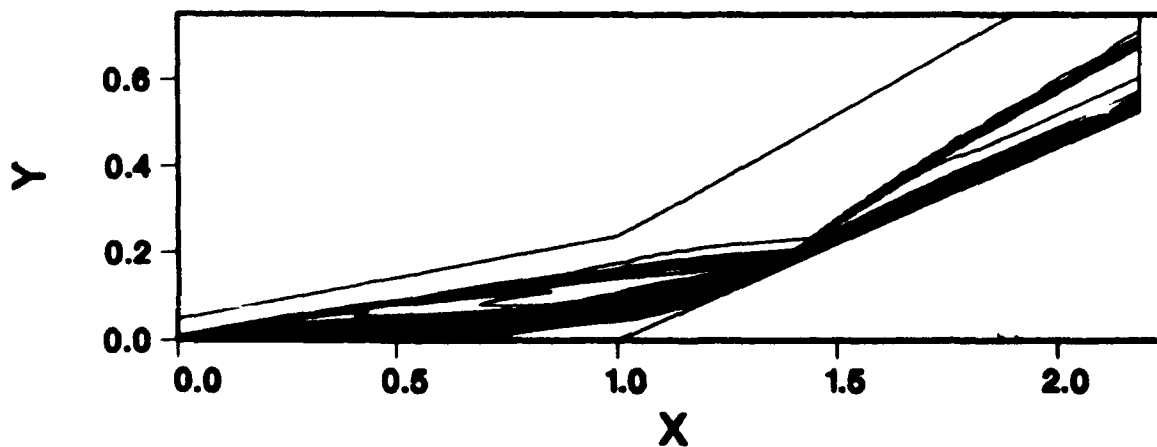


Figure 19: Mach contours for compression corner flow on Grid 4

by Rudy *et al.* for whom the peaks lie downstream of the experimental locations. The results of Rizzetta *et al.* with the CFL3D code indicate a higher sensitivity to vertical grid resolution than observed in the present research. Results with the Beam-Warming algorithm, the VAPOR code (based upon the OSW algorithm) and MacCormack explicit predictor corrector algorithm were also presented by Rizzetta *et al.*. On a grid identical to that denoted Grid 3 in the present research, the Beam-Warming and OSW algorithms exhibit significant underprediction in peak heat transfer while the MacCormack predictor corrector algorithm performs reasonably well. All the computations mentioned above, as also those reported by Thareja *et al.* [48] with the adaptive LAURA algorithm [48] fail to predict the dip in skin friction coefficient at about  $X/L \sim 1.25$ . The location of separation and reattachment points and extent of separation are compared in Table 5.2 for several research efforts.

Table 5.2: Separation region details for corner flow

Solution Algorithm		Separation Point	Reattachment Point	Total Extent
Experiment		0.5475-0.7025	1.1278-1.3748	0.5703-0.8273
CFL3D [48]		0.5318	1.3431	0.8113
Thareja <i>et al.</i> [48]		0.5588	1.3493	0.8113
MC	A	0.9813	1.0242	0.0429
	B	0.8929	1.1100	0.2171
	C	0.6516	1.2748	0.6232
	D	0.6596	1.2688	0.6092
vL	A	—	—	No sep. detected
	B	0.9274	1.1244	0.1970
	C	0.7703	1.2150	0.4446
	D	0.7733	1.2166	0.4432
Roe	A	0.9871	1.0173	0.0302
	B	0.9033	1.1226	0.2194
	C	0.7449	1.2367	0.4917
	D	0.7330	1.2381	0.5051

## 6. Conclusions

A detailed examination of the performance of several flux-split algorithms is attempted on two problems representative of complex flowfields. Results are compared with experimentally observed data. Based upon available results, the following conclusions are made:

- The method of MacCormack and Candler performs accurately for both the blunt body flow as well as the ramp flow insofar as both surface pressure and heat transfer are concerned. The overall accuracy is comparable to Roe's flux-difference split scheme and, in the present numerical framework, is more robust – permits code operation at higher CFL numbers leading to more rapid convergence.
- van Leer's scheme: This scheme displays a tendency to consistently overpredict heat transfer indicating perhaps excess diffusion in the boundary layer. However, with grid refinement, the accuracy of this method rapidly approaches those of the other two.
- Roe's flux difference scheme: This scheme exhibits a tendency toward the development of anomalous "carbuncle" solutions for blunt body flows. This tendency may be suppressed by appropriate increase in the eigenvalue cutoff required to enforce the entropy condition. For the corner flow, the performance of this scheme is comparable to the MC scheme.

Although the MC and Roe schemes exhibit excellent comparison with experimental data, this result is representative only at the flow parameters considered and may not carry over to other conditions. Further computations at higher Mach and Reynolds numbers are necessary. For corner flows, the present results indicate the need for further computations with higher streamwise resolution.

## 7. References

- [1] H.C. Yee, G.H. Klopfer, and J.-L. Montagne. High-Resolution Shock-Capturing Schemes for Inviscid and Viscous Hypersonic Flows. Technical Report 100097, NASA - Ames Research Center, Moffet Field, California, April 1988.
- [2] J.L. Steger and R.F. Warming. Flux Vector Splitting of the Inviscid Gasdynamic Equations with Application to Finite Difference Methods. *Journal of Computational Physics*, 40(2):263-293, April 1981.
- [3] B. van Leer. Flux-Vector Splitting For the Euler Equations. Technical Report 82-30, ICASE, September 1982.
- [4] R.F. Warming and R.M. Beam. Upwind Second-Order Difference Schemes and Applications in Aerodynamic Flows. *AIAA Journal*, 14(9):1241-1249, September 1976.
- [5] R.F. Warming and R.M. Beam. On the Construction and Application of Implicit Factored Schemes for Conservation Laws. In *Symposium on CFD*. SIAM-AMS, 1978.
- [6] R.W. MacCormack and G.V. Candler. The Solution of the Navier-Stokes Equations with Gauss-Seidel Line Relaxation. *Symposium in Honor of G. Moretti's 70th Birthday*, 1987.
- [7] H.C. Yee. A Class of High-Resolution Explicit and Implicit Shock-Capturing methods. Technical Report TM 101088, NASA, February 1989.
- [8] N. Kroll, D. Gaitonde, and M. Aftosmis. A Systematic Comparative Study of Several High Resolution Schemes for Complex Problems In High Speed Flows. *AIAA Paper 91-0636*, 1991.
- [9] H.C. Yee. Construction of Implicit and Explicit Symmetric TVD Schemes and Their Applications. *Journal of Computational Physics*, 68:151-179, 1987.
- [10] H.C. Yee. Upwind and Symmetric Shock-Capturing Schemes. Technical Report 89464, NASA-TM, 1987.

- [11] H.C. Yee and A. Harten. Implicit TVD Schemes for Hyperbolic Conservation Laws in Curvilinear Coordinates. *AIAA Journal*, 25:266-274, 1987.
- [12] B. van Leer. Towards the Ultimate Conservation Difference Scheme V, A Second-Order Sequel to Godunov's Method. *Journal of Computational Physics*, 32:101-136, 1979.
- [13] P.L. Roe. Approximate Riemann Solvers, Parameter Vectors and Difference Schemes. *Journal of Computational Physics*, 43:357-372, 1981.
- [14] P.G. Buning and J.L. Steger. Solution of the Two-Dimensional Euler Equations with Generalized Coordinate Transformation Using Flux Vector Splitting. *AIAA Paper 82-0971*, 1982.
- [15] G.V. Candler and R.W. McCormack. The Computation of Hypersonic Ionized Flows in Chemical and Thermal Nonequilibrium. *AIAA Paper 88-0511*, 1988.
- [16] D. Gaitonde and J. Shang. A Numerical Study of Viscous Shock-on-Shock Hypersonic Flows with a Modified Steger-Warming Flux Split Scheme. *AIAA Paper 90-1491*, 1990.
- [17] W.K. Anderson, J.L. Thomas, and B. van Leer. A Comparison of Finite Volume Flux Vector Splittings for the Euler Equations. *AIAA Paper 85-0122*, 1985.
- [18] W.K. Anderson, J.L. Thomas, and D.L. Whitfield. Multigrid acceleration of the flux split euler equations. *AIAA Paper 86-0274*, 1986.
- [19] J.L. Thomas and R.W. Walters. Upwind Relaxation Algorithms for the Navier Stokes Equations. *AIAA Paper 85-1501CP*, 1985.
- [20] J.L. Thomas, S.L. Taylor, and W.K. Anderson. Navier-Stokes Computations of Vortical Flows Over Low Aspect Ratio Wings. *AIAA Paper 87-0207*, 1987.
- [21] Y.J. Moon and M. Holt. Interaction of an Oblique Shock Wave with Turbulent Hypersonic Blunt Body Flows. *AIAA Paper 89-0272*, 1989.

- [22] B. van Leer, J.L. Thomas, P.L. Roe, and R.W. Newsome. A Comparison of Numerical Flux Formulas for the Euler and Navier-Stokes Equations. *AIAA Paper 87-1104*, 1987.
- [23] D. Levy, K. Powell, and B. van Leer. An Implementation of a Grid-Independent Upwind Scheme for the Euler Equations. *AIAA Paper 89-1931-CP*, 1989.
- [24] M-S. Liou and B. van Leer. Choice of Implicit and Explicit Operators For the Upwind Differencing Method. *AIAA Paper 88-0624*, 1988.
- [25] Y. Liu and M. Vinokur. Nonequilibrium Flow Computations. I. An Analysis of Numerical Formulation of Conservation Laws. *Journal of Computational Physics*, 83(2):373-397, August 1989.
- [26] B. Grossman and P. Cinnella. The Computation of Non-Equilibrium Chemically-Reacting Flows. *Computers & Structures*, 30(1/2):79-93, 1988.
- [27] B. Grossman and P. Cinnella. Flux-Split Algorithms for Flows with Non-equilibrium Chemistry and Vibrational Relaxation. *Journal of Computational Physics*, 88:131-168, 1990.
- [28] J-S. Shuen, M-S. Liou, and B. van Leer. Inviscid Flux-Splitting Algorithms for Real Gases with Non-equilibrium Chemistry. *Journal of Computational Physics*, 90:371-395, 1990.
- [29] E. von Lavante. Accuracy of Upwind Schemes Applied to the Navier-Stokes Equations. *AIAA J.*, 28(7):1312-1314, July 1990.
- [30] J. Fay and F. Riddell. Theory of Stagnation Point Heat Transfer Rate in Dissociated Air. *Journal of the Aeronautical Sciences*, 25(2), 1958.
- [31] K.M. Peery and S.T. Imay. Blunt-Body Flow Simulations. *AIAA Paper 88-2904*, 1988.
- [32] E. Josyula and J.S. Shang. Numerical Simulation of Nonequilibrium Hypersonic Flow with Adaptive Grid. *AIAA Paper 90-1490*, 1990.

- [33] M-S. Liou and C.J Steffen Jr. Development of New Flux Splitting Schemes. *CFD Compendium of Abstracts, Computational Fluid Dynamics Conference, NASA Ames Research Center*, page 26, March 1991.
- [34] M.S. Holden and J.R. Moselle. Theoretical and Experimental Studies of the Shock Wave-Boundary Layer Interaction on Compression Surfaces in Hypersonic Flow. Technical Report ARL 70-0002, Aerospace Research Laboratories, WPAFB, OH, January 1970.
- [35] D.P. Rizzetta and K.D. Mach. Comparative Numerical Study of Hypersonic Compression Ramp Flows. *AIAA Paper 89-1877*, 1989.
- [36] D.H. Rudy, J.L. Thomas, A. Kumar, P.A. Gnoffo, and S.R. Chakravarthy. Computation of Laminar Hypersonic Compression-Corner Flows. *AIAA Journal*, 29(7):1108-1113, July 1991.
- [37] R. MacCormack. Current Status of Numerical Solutions of the Navier-Stokes Equations. *AIAA Paper 85-0032*, 1985.
- [38] G.V. Candler. *The Computation of Weakly Ionized Hypersonic Flows In Thermo-Chemical Nonequilibrium*. PhD thesis, Stanford University, California, 1988.
- [39] J.L. Thomas, B. van Leer, and R.W Walters. Implicit Flux-Split Schemes for the Euler Equations. *AIAA Paper 85-1680*, 1985.
- [40] R.W. MacCormack. Solution of the Navier-Stokes Equations In Three Dimensions. *AIAA Paper 90-1520*, 1990.
- [41] A. Harten. High Resolution Schemes for Hyperbolic Conservation Laws. *Journal of Computational Physics*, 49:357-393, 1983.
- [42] R. Riedelbauch and G. Brenner. Numerical Simulation of Laminar Hypersonic Flow Past Blunt Bodies Including High Temperature Effects. *AIAA Paper 90-1492*, June 1990.
- [43] B. Müller. Simple Improvements of an Upwind TVD Scheme for Hypersonic Flow. *AIAA Paper 89-1977-CP*, 1989.



- [44] R.K. Prabhu, J.R. Stewart, and R.R. Thareja. A Navier-Stokes Solver for High Speed Equilibrium Flows and Application to Blunt Bodies. *AIAA Paper 89-0668*, 1989.
- [45] G.H. Klopfer and H.C. Yee. Viscous Hypersonic Shock-On-Shock Interaction on Blunt Cowl Lips. *AIAA Paper 88-0233*, 1988.
- [46] M.S. Holden, A.R. Wieting, J.R. Moselle, and C. Glass. Studies of Aerothermal Loads Generated in Regions of Shock/Shock Interaction in Hypersonic Flow. *AIAA Paper 88-0477*, 1988.
- [47] H.W. Liepmann and A. Roshko. *Elements of Gasdynamics*. John Wiley and Sons, Inc., New York, 1963.
- [48] R.R. Thareja, R.K. Prabhu, K. Morgan, J. Peraire, J. Peiro, and S. Soltani. Applications of an Adaptive Unstructured Solution Algorithm to the Analysis of High Speed Flows. *AIAA Paper 90-0395*, 1990.

## Nomenclature

$A$	flux Jacobian of $F$
$B$	flux Jacobian of $G$
$Btu$	British Thermal Units
$c$	stretch factor; local speed of sound
$C$	component of $Q$
$C_v$	specific heat at constant volume
$CFL$	Courant-Friedrich-Levy number
$e$	total energy
$e_i$	internal energy
$f$	feet
$F, \hat{F}, G, \hat{G}$	flux vectors
$G.R.$	global residual
$IL, JL$	points in $\xi$ and $\eta$ direction
$J$	Jacobian, inverse cell volume
$L$	distance from leading edge to corner
$M$	Mach number
$MC$	MacCormack and Candler scheme
$n$	normal direction
$n_{it}$	number of iterations to double CFL
$OSW$	Original Steger Warming scheme
$p$	pressure
$psi$	pounds per square inch
$Pr$	Prandtl number
$PR$	pressure function

$Q$	matrix diagonalizing $A$
$R$	gas constant; Rankine
$Re$	Reynolds number
$RMS P$	root mean square surface pressure
$RMS Q$	root mean square surface heat transfer
$S$	Jacobian of $V$ with respect to $U$
$t$	time
$T$	temperature
$u$	Cartesian velocity in $x$ direction
$U, \hat{U}$	solution vector
$v$	Cartesian velocity in $y$ direction
$\vec{v}$	Cartesian velocity vector
$vL$	van Leer scheme
$V$	vector of primitive variables
$W$	vector of extrapolated variables
$x, y$	Cartesian coordinates
$\delta$	cutoff value; any change
$\tilde{\delta}$	cutoff parameter
$\Delta$	shock standoff distance
$\nabla$	gradient operator
$\gamma$	ratio of specific heats
$\lambda$	eigenvalue
$\partial$	partial derivative operator

$\rho$	density
$\theta$	angle
$\xi, \eta$	transformed coordinates
$X_i$	pressure switch

### Subscripts

$j + \frac{1}{2}$	interface between $j$ and $j + 1$
$v$	viscous
$w$	wall
$\infty$	freestream conditions

### Superscripts

$L$	state at left of interface
$R$	state at right of interface
$+, -$	positive and negative components